Design and setup of an optical experiment for searching for weakly interacting sub-eV particles (WISPs) that couple to an electro- and/or magnetic field

Von der Fakultät für Mathematik und Physik

der Gottfried Wilhelm Leibniz Universität Hannover

zur Erlangung des akademischen Grades

DOKTOR DER NATURWISSENSCHAFTEN

Dr. rer. nat.

genehmigte Dissertation

von

Dipl.-Phys. Robin Holger Helmut Bähre

2017

Contents

List of Acronyms

AA   automatic alignment

AOM   acousto-optical modulator

ALP   axion-like particle

ADMX   Axion Dark Matter Experiment

CBB   central breadboard

EOM   electro-optical modulator

FFT   fast Fourier transform

LIGO   Laser Interferometer Gravitational Wave Observatory

LSW   Light-shining-through-a-wall

MOPA   master oscillator power amplifier

PC   production cavity

PD   photo-detector

QCD   quantum chromo-dynamics

QPD   quadrant photo-detector

RC   regeneration cavity

RIN   relative intensity noise

SHG   second harmonic generation

SM   Standard Model of particle physics

WISP   weakly interacting sub-eV particle

List of Figures

Note: all data, plots and information on measurements is stored in a personal archive. The data can be request by the author acronym 'robaeh' and the plot number in this list.

Abstract

The subject of this thesis is design, implementation and results of the optical setup for ALPS-II. ALPS-II is a cavity-enhanced light-shining-through-a-wall experiment searching for weakly interacting sub-eV particles (WISPs).

The possible existence of WISPs is well-motivated from quantum chromo-dynamics (QCD) and string theory. Moreover, the discovery of a particular member of the WISP family, the *QCD axion* proposed by Peccei and Quinn, would explain why for the strong interaction no CP violating terms could be measured so far, the so called *strong CP problem.*

A light-shining-through-a-wall experiment strives to probe the existence of WISPs by exploiting their coupling to photons. To produce and detect WISPs experimentally, a strong light field is send towards a wall that is opaque to photons but transparent to WISPs, which exhibit a vanishing interaction cross-section with ordinary matter. If WISPs couple to the light beam they can transverse the wall and by the inverse process produce a small photon flux on the other side of the wall that can be detected with a sufficiently sensitive photon detector. For spin-0 WISPs, also the presence of a magnetic field is required.

To overcome the difficulty of probing WISPs with small coupling constants, for which their existence could not be experimentally excluded so far, not only strong magnetic fields, long interaction distances and low noise photon counters, but also sophisticated optical techniques are required.

The ALPS-II design relies on two optical cavities resonantly enhancing the production field on one side of the wall and the regenerated photon field on the other side. For small ALP masses as they are tackled in the ALPS-II search, the coherent properties of the production field are effectively maintained in the conversion and reconversion process. If the resonant conditions for the cavities on both sides of the wall are maintained, the number of rege-

nerated photons is enhanced by the product of the cavities build-up factors and therefore a striking improvement of the overall sensitivity of the WISP search can be achieved.

The goal of the ALPS-II experiment is to set up two 100 m long cavities within a serial configuration of superconducting HERA dipole magnets. A build-up factor of $5,000$ for the production side and a build-up factor of $40,000$ for the regeneration side are aimed for. Maintaining the resonance conditions for the high-finesse cavities with respect to the laser beam and with respect to each other during the measurement requires a robust setup and active control of cavity length and alignment.

A frequency/length stabilization with Pound-Drever-Hall (PDH) sensing and an automatic alignment control employing differential wavefront sensing (DWS) have been setup for two pre-stages of the final ALPS-II experiment. First of all, a table-top prototype setup at the Albert-Einstein-Institute in Hannover with 1 m long cavities to demonstrate the fundamental ideas of the ALPS-II design. And in addition, a setup that provides space for two 10 m long cavities in a HERA Hall at the Deutsche Elektronen Synchrotron (DESY) in Hamburg which resembles the conditions for the final ALPS-II design more closely.

Moreover, the application of a unique technique, the dichroic lock, will be described. It is presented as a solution to stabilize the cavity on the regeneration side to a virtual 1064 nm mode by locking it to a light beam of the second harmonic frequency while keeping the cavity clear of infrared light.

For this thesis work, electronics and optical setups have been designed and employed for characterization and frequency and alignment control of the ALPS cavities.

Keywords: WISPs, ALPS-II, resonant photon regeneration

Kurzzusammenfassung

Das Thema dieser Dissertation sind Entwurf, Umsetzung und Resultate eines optischen Aufbaus für ALPS-II. ALPS-II ist ein resonator-gestütztes Licht-durch-die-Wand-Experiment zur Suche nach weakly interacting sub-eV particles (WISPs).

Die mögliche Existenz von WISPs ist gut motiviert durch QCD und Stringtheorie. Darüber hinaus würde die Entdeckung eines bestimmten Teilchens der WISP-Familie, des QCD-Axions, das von Peccei und Quinn vorhergesagt wurde, erklären, warum eine Verletzung der CP-Symmetrie experimentell nicht gemessen wurde.

Ein Licht-durch-die-Wand-Experiment versucht, die Existenz von WISPs nachzuweisen, in dem ihre Kopplung an Photonenfelder ausgenutzt wird. Um WISPs experimentell zu erzeugen und nachzuweisen, wird ein starker Lichtstrahl auf eine Wand gerichtet, die undurchlässig für Photonen ist, die für WISPs jedoch aufgrund ihres verschwindenden Wechselwirkungsquerschnitts mit herkömmlicher Materie durchlässig ist.

Um die Schwierigkeit zu bewältigen, WISPs mit geringen Kopplungskonstanten nachzuweisen, deren Existenz nicht experimentell ausgeschlossen worden ist, werden nicht nur starke Magnetfelder, lange Welchselwirkungsstrecken und Photonenzähler mit geringem Dunkelrauschen benötigt, sondern auch anspruchsvolle optische Verfahren.

Das Konzept von ALPS-II beruht auf einem optischen Resonator vor der Wand, der das Produktionsfeld resonant überhöht und einem auf der anderen Seite der Wand, der das regenerierte Feld verstärkt. Für ALPs mit geringer Masse, wie sie das ALPS-II-Experiment zum Ziel hat bleibt die Kohärenz des Lichts bei Konversion und Rückkonversion erhalten. Wenn die Resonanzbedingungen für beide Resonatoren erfüllt sind, wird die Anzahl der regenierten Photonen mit den Überhöhungsfaktoren beider Resonato-

ren verstärkt. Daher kann eine erhebliche Verbesserung der Sensitivität der WISP-Suche erreicht werden.

Das Ziel des ALPS-II-Experiments ist es, zwei 100 m lange optische Resonatoren in einer seriellen Anordnung von HERA-Dipol-Magneten aufzubauen. Ein Überhöhungsfaktor von 5.000 auf der Produktionsseite und 40.000 auf der Regenerationsseite werden angestrebt. Um die Resonanzbedingungen der Resonatoren untereinander und in Bezug auf das einfallende Laserlicht aufrecht zu erhalten, werden ein robuster Aufbau und eine aktive Stabilisierung von Resonatorlänge und -justage benötigt.

Eine Frequenzstabilisierung im Pound-Drever-Hall-Verfahren und eine automatische Justageregelung mit differenzieller Wellenfronterfassung wurden aufgebaut für zwei Vorstufen des ALPS-II-Experiments. Zunächst ein Prototypenaufbau mit 1 m-langen Resonatoren im Laserlabor des Albert-Einstein-Institutes in Hannover mit dem Ziel, die grundlegenden Techniken des ALPS-II-Konzepts zu zeigen. Sodann ein Aufbau, der Platz für zwei 10 m lange Resonatoren in der HERA-Halle am Deutschen Elektronen-Synchrotron (DESY) bietet, der den Bedingungen des endgültigen ALPS-II-Aufbaus stärker entspricht.

Außerdem wird eine besondere Technik beschrieben, der dichroitische Lock, der als Lösung für die Stabilisierung des Regenerationsresonators auf infrarotes Licht vorgestellt wird, bei der dieses selbst nicht in diesen Resonator gelangt.

Für diese Arbeit wurden elektronische Geräte und optische Aufbauten entwickelt und angewendet für Charakterisierung, Frequenz- und Justageregelung der ALPS-Resonatoren.

Schlagwörter: WISPs, ALPS-II, resonante Photonenregeneration

Chapter 1

The Search for WISPs

1.1 Introduction

The Standard Model of particle physics (SM) is an aggregation of our knowledge of the elementary particles and their interactions through the fundamental forces [18].

Just like at the turn of the century, Max Planck's pursuit of overcoming the riddle that has been posed by what at this time was considered an ultraviolet catastrophe stood at the cusp of modern quantum physics and only five years later the formulation of special relativity by Albert Einstein had put an end to the reign of Newton's theory of gravitation, it was in 1957 when the classical view of a particle universe that was governed by the order of three fundamental symmetries – charge (C), parity (P) and time (T) – began to totter. The discovery of maximum parity violation in the weak force questioned classical laws of physics. However, it was not until 1964, that James Cronin and Val Fitch [7] showed that even the combined symmetry of charge and parity (CP) was violated by the weak force and could no longer be considered a fundamental principle of nature.

The current formulation developed over the course of the last 60 years and arriving at an inherently complete and consistent model marked a great success. It led to the prediction of a number of new particles, which indeed could be discovered one after another, with the final candidate the Higgs boson [19] only recently [24].

Although one might expect that the perception that these classical symmetries only have limited validity and do only hold for some of the funda-

mental forces or for low energy levels, would have made symmetries as a basic idea in physics less prominent, quite the contrary was true. Not only was the combined symmetry of CPT found to be obeyed by all fundamental forces in the SM, its potential violation was also postulated to imply a violation of Lorentz invariance [14]. Symmetries in general still play an important role in our comprehension of physics.

This is exemplified when the breaking of symmetries is linked to the existence of bosons as in case of the massless Goldstone bosons that appear as a consequence of spontaneous symmetry breakdown and the Higgs mechanism being linked to electroweak symmetry breaking.

A particularly interesting case for the motivation of the ALPS experiments is the spontaneous breaking of the Peccei-Quinn symmetry. The Peccei-Quinn theory was proposed to explain why the QCD Lagrangian contains a CP violating parameter θ, but although this parameter can have values from 0 to 2π, in a measurement of the electric dipole moment of the neutron this value was not found to deviate from 0 with an uncertainty better than 10^{-10} [8]. Because the ambiguity of this finding, called the strong CP problem, was unsatisfying, it was speculated that this apparent coincidence was in reality founded in a new symmetry, which was proposed by Helen Quinn and Roberto Peccei in 1977 [28].

A descriptive consequence of this theory that could resolve the strong CP problem is the existence of a new particle, the axion. The QCD axion is predicted as a light-weight, very weakly coupled and long-lived pseudoscalar boson [27] not included in the SM.

These properties made the axion a prominent candidate to solve other unresolved questions in physics, first of all the dark matter problem [10]. Additionaly, a more general formulation also allowed for other axion-like particles not necessarily linked to the Peccei-Quinn theorem [33]. All of them have been summed up in the family of weakly interacting sub-eV particles (WISPs).

Astrophysics gives some hints that the idea of axions and ALPs might not only be of theoretical interest.

The most striking allusion to a possible need for an extension of the SM is the amount and distribution of what has been titled dark matter and dark energy in our universe. The different portions of the mass-energy in our universe have been determined with growing precision in several surveys, re-

cently by the analysis of cosmic microwave background in the Planck mission [29]. The results conclude that only 4.9 % of matter in our universe is baryonic while 26.8 % are attributed to dark matter and 68.3 % to dark energy. The demand for these huge dark fractions of mass-energy that erased from these observations has until now overcome all attempts to be successfully incorporated in the SM. Axions and axion-like particles could well match the properties of cold dark matter (CDM) and moreover, are likely to be produced by thermal processes and misalignment mechanism in the early universe. [32].

Other astrophysical hints that support the existence of ALPs are the anomalous strong transparency of the universe for TeV photons [23] and the luminosity of white dwarfs [22].

1.2   WISP searches

Many discoveries of new particles that make up the matter in our universe and also various tests of the SM have been conducted using particle accelerators providing particles with ever higher energies for collision experiments. However, in the search for WISPs, large accelerators are not the method of choice. This is because the generation of these particles that exhibit sub-eV energies and marginal interaction with other particles cannot efficiently be accomplished with high-energy collisions.

The nature of the hypothetical ALP hints to another way to probe its existence. A wide band of experiments is based upon the so-called Primakoff effect, which substantiates a coupling of the axion to two photons respectively one photon in an electro-magnetic background [31]. Typically, the case of a laser photon with frequency ω is considered that is travelling a distance L along the x-axis in a magnetic field $\vec{B} = \hat{e}_z B f(x)$ perpendicular to its propagation direction and with spatial variation $f(x)$. The conversion probability $P_{\gamma,a}$ to an axion with mass m_a can then be expressed by the formula [2]

$$P_{\gamma,a} = \frac{1}{4} \frac{\omega}{\sqrt{\omega^2 - m_a^2}} (gBL)^2 \left| F(qL) \right|^2 \qquad (1.1)$$

where g is the coupling constant provided by the interaction term of the

respective Lagrangian and $F(qL)$ is the form factor defined as

$$F(qL) = \frac{1}{L} \int_0^L dx' f(x') e^{iqx'} \qquad (1.2)$$

with q the momentum transfer to the magnetic field.

Other ALPs like the hidden-sector photons (HP) are able to couple to photons via kinetic mixing [1].

A large number of experiments searching for WISPs can be summarised in a few groups by their search strategy. Haloscopes like the Axion Dark Matter Experiment (ADMX) are looking for relic axions that arose in the early universe [35]. Helioscopes focus on the ALPs that are produced by the strong electric and magnetic fields in the sun. The helioscope CAST has set strong bounds on the existence of ALPs [9]. Light-shining-though-a-wall experiments search for WISPs that are produced in the laboratory and will be discussed in more detail in the following chapter. A good review of the different types of WISP searches can be found in [3].

1.3   Light-shining-though-a-wall

This coupling can be exploited to attribute the production and the detection of the wispy ALPs to that of a highly disposable quantity – the electro-magnetic field.

In its most comprehensive way, this idea is carried out in a light-shining-through-a-wall type of experiment.

This refers to a type of experiment, where strong light fields are directed towards a wall that is opaque to photons but transparent to the weakly interacting ALPs in an environment providing an electro-magnetic background field orthogonal to the direction of light propagation. In this setup, the arrival of photons at the otherwise dark region beyond the wall proofs the existence of the ALP as a mediator between the electro-magnetic fields – the production field on one side of the wall and the observed regenerated field on the other side.

1.4 The ALPS experiment

In the quest for ALPs and HPs, the ALPS collaboration follows an all-laboratory LSW approach. This implies that no external WISP sources are required in the search and therefore modelling of and adaptation to these sources are dispensable.

However, the small magnitudes of the photon-WISP coupling on which the existence of ALPs is tested represents a tremendous challenge for this kind of WISP searches. This holds especially true for all-laboratory searches because these incorporate the photon-WISP coupling twice in their search strategy: once for the generation of WISPs and once for the subsequent detection of reconverted photons.

On the contrary, the use of coherent laser light as a primary light source offers many advantages in the production, conversion and detection process that can be exploited to widely improve the sensitivity of the LSW setup.

In the following, the sensitivity of an LSW experiment will be illustrated and a brief review will be held on the first ALPS experiment conducted by the ALPS group.

In 2009, the ALPS collaboration conducted a WISP search using an LSW type of experiment inside a single superconducting HERA dipole magnet with a field intensity of $B = 5.3$ T and a length of 8.8 m.

The primary light power for the production of WISPs was provided by a 35 W master-oscillator power amplifier (MOPA) laser with a wavelength of 1064 nm. However, the lacking availability of affordable low dark noise single photon detectors in the infrared spectrum, required a conversion of the optical power to the visible region which was accomplished by second harmonic generation in a PPKTP crystal providing up to 5 W of green light with 532 nm wavelength.

While similar LSW experiments have been conducted earlier, the ALPS experiment was able to improve the sensitivity for laboratory searches by amplifying the available primary photon flux with a production cavity (PC). Although no WISP particles were found during the measurement, this enabled the experimenters to reached unprecedented sensitivity for laboratory ALPs and HP searches in a wide mass range and to improve exclusion limits for the ALP to coupling rates $g < 5 \cdot 10^{-7}$ GeV^{-1} for masses $m \leq 0.5$ meV [11].

Chapter 2

ALPS-II

2.1 Resonant enhancement of WISP production and photon regeneration

The photon-to-axion conversion probability $P_{\gamma,a}$ (cf. (1.1)) marks in general a determining quantity in the characterization of a photon regeneration experiment. Together with the available primary optical power and the efficiency of single photon detection it fundamentally limits the overall sensitivity of the experiment.

However, it was already proposed by Hoogeveen and Ziegenhagen [21] that the electric field that contributes in the production of axion-like particles can be largely increased by the application of an optical resonator on the left side of the wall. This resonator is also referred to as the production cavity (PC).

The effective number of photons in the production region is increased by
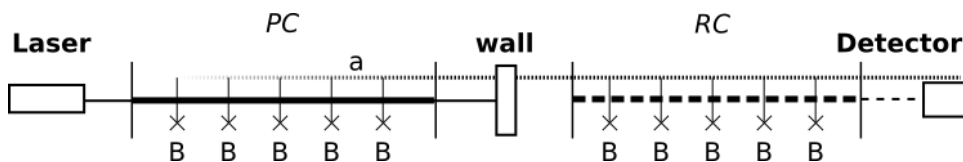
Figure 2.1: Principle sketch of a photon regeneration experiment with resonantly-enhanced production and regeneration.

the build-up factor [26]

$$\beta_{PC} = \frac{4 \cdot T_{PC,1}}{(T_{PC,1} + T_{PC,2} + A_{PC})^2} \,, \qquad (2.1)$$

where $T_{PC,1}$ is the power transmission of the input coupler, $T_{PC,2}$ the power transmission of the output coupler and A_{PC} are the additional round trip losses of this cavity, e.g. due to absorption, scattering or aperture effects. The number of axion-like particles generated in the production region and the number of regenerated photons are consequently increased by the same factor.

Mueller et al. also point out that the build-up of the photon field in the production region – as in the case of the PC – due to its coherence also offers the opportunity to enhance the gain for the signal field in the regeneration region with a resonant build-up. This build-up can be achieved when an optical resonator on the right side of the wall – the regeneration cavity (RC), see fig. 2.1 – matches the resonance condition for the regenerated photons $\phi_{RT} = 2\pi N$, where ϕ_{RT} is the round-trip phase of the photon field [26].

If phase and spatial distribution of the regenerated photons exactly match the mode of the RC, the number of photons leaking out of the cavity is now again increased by the build-up factor

$$\beta_{RC} = \frac{4 \cdot T_{RC,1}}{(T_{RC,1} + T_{RC,2} + A_{RC})^2} \qquad (2.2)$$

with $T_{RC,1}$ in comparison to the case without RC. For a photon regeneration experiment with resonant enhancement on production and regeneration side, the total number of photons in the signal field N_S is then given by

$$N_S = \beta_{PC}\beta_{RC}\eta^2 P_{\gamma,a}^2 N_{in} \,, \qquad (2.3)$$

where N_{in} denominates the number of photons entering the PC and η the spatial overlap of the modes of photon and WISP field. For $m_{\mathrm{a}} \ll \omega_0$, this is identical to the overlap integral of the two cavity modes [26].

2.2   Photon and WISP field coupling

In summary, equation 2.3 demonstrates that the total number of regenerated photons can be largely improved by resonant optical build-up of the photon

fields. To evaluate the actual effect on the expected signal fields the overlap factor η has to be taken into account.

An optical cavity will only enhance the production light field when the frequency of the incident laser beam matches the resonance frequency and the Eigenmode of the cavity and otherwise will act as a spatial and spectral filter. The same holds true for the regeneration cavity with respect to the regenerated photon field. However, the resonance conditions for the enhancement of the regenerated field before its subsequent detection are difficult to maintain because electromagnetic fields injected for the cavity readout shall not perturb the measurement of the regenerated signal. This will be discussed in 2.2.2.

It is important to recognize that only the electromagnetic fields are confined in this setup. The presumed WISP fields freely propagate in space as they do hardly interact with matter. However, they play a mediating role between the production mode and the regenerated mode that is required to be aligned towards the regeneration cavity.

2.2.1 Achieving and maintaining coupling of the optical modes

As discussed above, putting certain limits on the fluctuation of coupling constants between the electro-magnetic field modes of the laser, the production cavity and the regeneration cavity can be directly translated into requirements on frequency and alignment stability of the cavities.

The dynamics of these variable are known to be driven by multiple factors. Among others, acoustic and seismic vibrations will shake mirror mounts and optical substrates. Also temperature-based expansion or shrinkage of opto-mechanical devices, laser tables, vacuum vessels and support structures will occur. The interrelation between these effects is causing uncorrelated and random fluctuations of the position and orientation of the reflective optical surfaces.

The concept pursued in ALPS-II to reduce the impact of these effects on the crucial optical components is manifold. It comprises of a rudimentary seismic isolation setup, the mounting of central optical components including the planar cavity mirrors on a rigid aluminium plate, referred to as the central breadboard (CBB), and an active control of the cavity length which is conducted such that the low noise background of the single-photon detector

is not spoiled with spurious photons.

2.2.2 Dichroic lock for length stabilization of the regeneration cavity

Optical resonators often require active control of their perimeter length in order to match the frequency of the incident light to the cavity's resonance frequency. This holds particularly true for the high-finesse ALPS-II cavities as the their bandwidth is very small.

With the Pound-Drever-Hall technique [4], a well-proven detection scheme is at hand to read out the relative frequency changes between an incident beam and the resonant axial mode of an optical cavity. The signal remains valid and linear for frequency offsets well below the cavity linewidth. With this sensing, an active stabilization of the laser frequency to the production cavity resonance frequency can be set up.

However, eliminating relative frequency fluctuations between the production and regeneration cavity poses additional challenges due to the specific topology of the LSW layout. It is required that all light from the production field is prevented from entering the regeneration region. This directly conflicts with the application of PDH sensing inside the RC.

To tackle this problem, different solutions have been suggested. Mueller et al. [26] proposed to apply a heterodyne readout technique for the regenerated photon flux which would not conflict with PDH sensing. The ALPS collaboration is following another approach in ALPS-II, which is going to implement a dichroic control scheme sensing the spatial and spectral position of the RC Eigenmode with second harmonic light fields [6].

The control scheme of the RC is using a low-power green, frequency-doubled control beam converted by a non-linear crystal from a pickoff of the primary light. The green light is later spectrally separated from the infrared signal mode in front of the detector.

The spatial and spectral overlap of the PC and RC mode can be verified by opening a shutter inside the central wall. The substrates on the optical axis of the cavities are arranged such that refractive changes to the beam axis between both inner cavity end-mirrors cancel out and therefore ensure that the PC mode will be perfectly aligned with the hypothetical WISP mode again, when arriving the RC input coupler.

Opening then shutter also allows to measure the differential phase of

green and infrared light in the RC caused by unequal penetration depth of the dielectric coating layers, which can then be corrected for by acousto-optical modulation of the green beam.

Alignment control

The acousto-optical modulation of the green beam is performed outside the vacuum vessel. Because the beam path is quite long and is partly located in air, the green mode incident on the RC can be subject to significant pointing fluctuations.

Alignment fluctuations of the laser beam towards the PC and RC mode are inducing power fluctuations on fields inside the cavity. While for the infrared laser beam incident on the PC this obviously harms the power stability of the circulating light, the case for the green auxiliary beam used for stabilizing the RC is different, since power fluctuations of the green light do not directly affect the power build-up of the infrared mode. The PDH detection scheme is known to be rather insensitive to power fluctuations of the readout beam. However, strong fluctuations also change the loop gain of the dichroic lock significantly and should therefore be avoided to achieve a stable lock.

For the ALPS-II experiment an automatic alignment technique for the PC and RC is employed that relies on differential wavefront sensing (DWS), which is also used in gravitational wave detectors [15].

2.2.3 Central Breadboard

Accurate collinear alignment of the PC and RC mode at any time during measurement is an important issue (see 2.4.1). While direct measurement of the mode overlap during operation is not possible, because the wall obstructs the transmitted beam of the PC from entering the RC, it is particularly helpful to align the cavity modes collinearly in a permanent fashion. Both cavities are designed to have a planar end-mirror on one side. The cavity mode axis is defined to represent a normal to its highly-reflective surface. Therefore, fixing both planar end-mirror in parallel on a rigid surface will force the cavity axes to be parallel too.

The ALPS-II design makes use of this fact and uses an aluminium bread-board which was commercially milled to give it an extra flat top surface (see
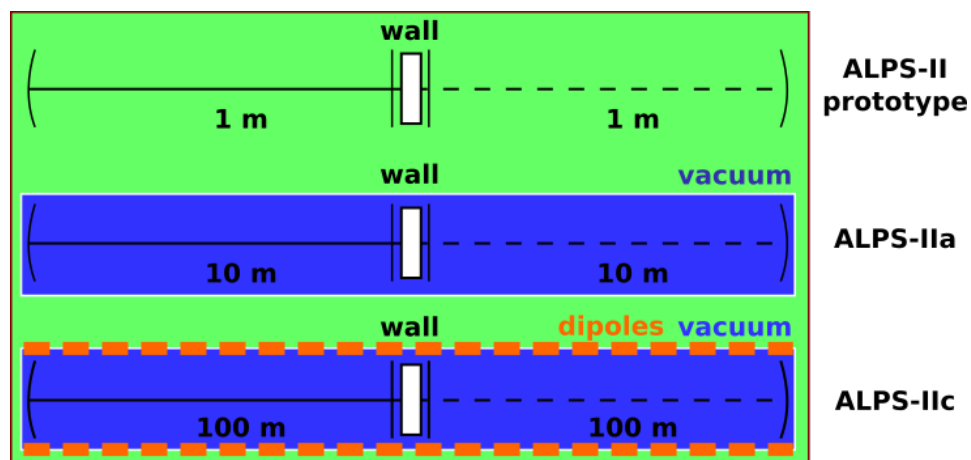
Figure 2.2: Stages of the ALPS-II experiment.

3.1.1). The substrates for the planar end-mirrors are then directly clamped on top of the board, which minimizes tilt of the two mirror with respect to each other. A minimization of the differential rotation has to be achieved by other means before clamping.

2.3 Stages of the ALPS experiment

The ALPS-II experiment is planned to be realized in different stages. This approach accommodates the restricted availability of infrastructure and personnel. While only the final stage will reach the full sensitivity, the development will continue during all stages and give practical and technical insight.

The final stage will be referred to as ALPS-IIc and involve a setup with two 100 m long cavities each enclosed in a serial string of ten super-conductive HERA dipole magnets. An intermediate stage is called ALPS-IIa. It comprises two 10 m long cavities without magnets and allows for hidden photon searches. A 1 m prototype experiment in Hannover is designed for development and testing of the cavity control scheme. Plans for a previously designated implementation of another intermediate stage called ALPS-IIb have currently been suspended.

In the following paragraphs, the particular stages will be presented in more detail.

2.3.1   1 m prototype

This prototype setup with two 1 m long cavities operated in air is designed for developing and testing electronic devices for cavity control, optical modulation and beam steering as well as acquiring experience in the optical set-up and identifying practical challenges. The cavities are not only smaller in size, but compared to ALPS-IIa and ALPS-IIc also have a reduced build-up of 100. In contrast to the ALPS-IIa and ALPS-IIc stage, this scale allowed for the experiment to be setup on a single laser table, located at the AEI facilities in Hannover. Components that were not immediately required for the operation of the optical cavities as a automatic shutter device and the single photon detector have been omitted.

2.3.2   ALPS-IIa

The ALPS-IIa laboratory in the HERA West hall on the DESY site provides sufficient space for the realization of two sequential 10 m long cavities enclosed by steel tubes allowing for in-vacuum operation.

It aims to fully demonstrate all features of the optical setup, which include cavity locking and automatic alignment control, tuning of the fixed frequency offset between the PC and RC and a light tight wall with a shutter that obstructs the infrared beam towards the RC. Just like in ALPS-IIc, the optical components are setup on three independently isolated laser tables. It also provides a testbed for the development of the TES detector.

The requirements for achieving a certain overlap between the optical modes are slightly reduced with respect to the ALPS-IIc stage due to shorter cavity size and beam waist diameter. The goals for the cavity build-up factors and coupling efficiency are equivalent to those of ALPS-IIc. Finally, this stage can be used to perform an in-laboratory science run searching for hidden-sector photons with unprecedented sensitivity.

2.3.3   ALPS-IIc

This stage of the experiment strives for an all-laboratory search for axion-like particles and hidden photons with unprecedented sensitivity.

A configuration of ten super-conductive HERA dipol magnets on each side of the wall will be arranged in the HERA tunnel. Since most of the HERA dipoles have been used in curved segments of the HERA ring before,

their beam pipes have been bent accordingly. To maximize the free clear aperture of the vacuum beam pipes through the dipole string to about 50 mm in diameter, each magnet is to be straightened prior to its installation by brute-force deformation applied to its outer vessel [6]. 100 m long cavities will be set up within the beam pipes on each side of the wall with a beam radius of 8.6 mm at the waist position. The cavities are designed to achieve a power build-up of $\beta_{PC} = 5,000$ for the *PC* and $\beta_{RC} = 40,000$ for the *RC*.

Of the different experimental stages, ALPS-IIc places the strictest requirements on the control of the cavity modes for obtaining the spectral and spatial overlap between the PC and RC mode. The large beam waist radius of 8.6 mm makes the alignment very susceptible to tilt. The high finesse of the cavities and the long round-trip distances nail down the acceptable relative frequency changes to only 1.5 Hz. The requirements on the optical design of ALPS-II will be discussed at length in 2.4.

Operating the optical cavities in vacuum tubes located inside the bore of the HERA dipole magnets poses additional challenges for the optical design, namely aligning and maintaining the cavity mode axis to the center axis of the beam pipe. This is even more difficult because for the experimenters access to the cavity mode is impossible within the magnets.

The operation of ALPS-IIc would not only allow for a detection of a potential flux of reconverted photons, but would also enable to conduct further research on the origin of the discovered signal photons. This can be done by introducing a frequency offset or slight misalignment between the *PC* and *RC* to discriminate between the dark flux and signal flux at the detector. It is also possible to turn the magnetic field on and off to decide whether a signal is originating from ALPs or from hidden photons.

Further discrimination can be made in case of an ALPs related signal by rotating the polarization of the production light with respect to the magnetic field. While the production of scalar ALPs require a magnetic field component perpendicular to the polarization of the incident light, pseudo-scalar ALPs are dependent on the magnetic field component that is directed parallel to the polarization of the light [6]. Other WISPs mixing kinetically with photons do not depend on the magnetic field. By rotation of the production light linear polarization, the effect on a possible signal can be investigated.

Increasing the optical density in the vacuum pipes by injecting small amounts of gas into the vessel, would slightly change the response to WISPs

with certain masses and therefore allow to probe for particles in a mass region which would otherwise be masked and also, to narrow down the mass range of WISPs that evoke a signal on the detector.

2.4 Requirements

2.4.1 Alignment

In both cases, for the PC and the RC, it is important to quantify the alignment losses due to mismatch of the incident beam. While effectively, the optical axes of the cavity mode as well as of the incoming field can change their position and bearing in space, we use the freedom of choice to define the cavity mode as the spatial reference and subsequently consider movement of the incident field in coordinates of the cavity.

To approximate the effect of relative beam position fluctuations (pointing), the beam position can be specified by a horizontal offset Δx, vertical offset Δy, a tilt angle θ_x in the horizontal plane (yaw) and a tilt angle θ_y in the vertical plane (pitch) around the beam waist position. We can now introduce the complex beam parameters ϵ_x and ϵ_y representing the beam misalignment.

$$\epsilon_x = \frac{\Delta x}{w_0} + i \cdot \frac{\theta_x}{\Theta_D}, \ \ \epsilon_y = \frac{\Delta y}{w_0} + i \cdot \frac{\theta_y}{\Theta_D} \tag{2.4}$$

For epsilon parameter $|\epsilon| \ll 1$, the coupling to TEM modes with mode index of more than 1 can be neglected. In this case, the coupling coefficient is approximated by

$$\eta \approx 1 - |\epsilon|^2$$

Evaluating these coupling terms it becomes obvious that with growing mode radius the coupling becomes more susceptible to tilt misalignment and less to transversal offsets. For cavities with beam waist diameters according to the parameters of the 1 m prototype setup, ALPS-IIa and ALPS-IIc, the results of an analysis on the coupling of a misaligned Gaussian mode to a cavity depending on the lateral shift or tilt around the beam waist can be found in figs. 2.3 and 2.4.
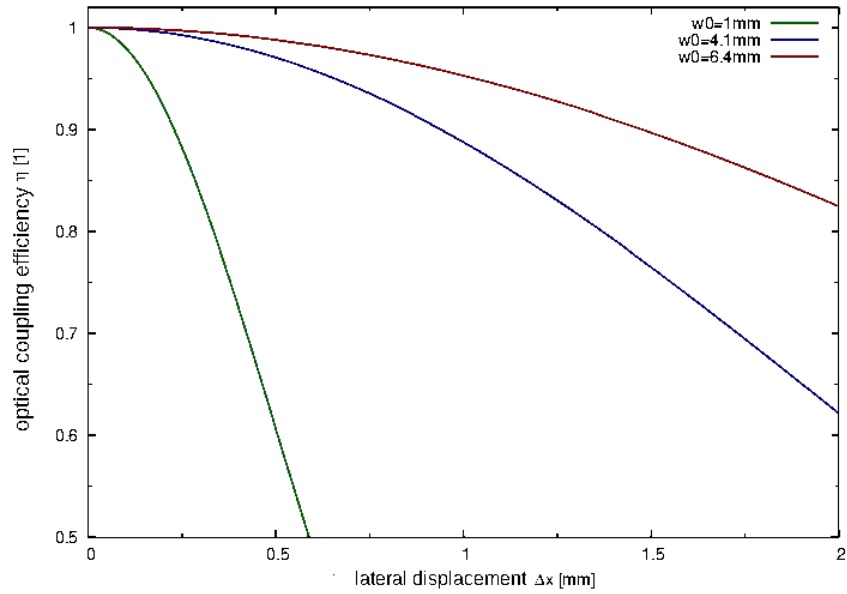
Figure 2.3: Coupling efficiency of a misaligned incident mode laterally shifted by Δx from the axis of the ALPS-II cavities with $w_0 = 1.0\,\text{mm}$ (green), $w_0 = 4.1\,\text{mm}$ (blue) and $w_0 = 6.4\,\text{mm}$ (red).
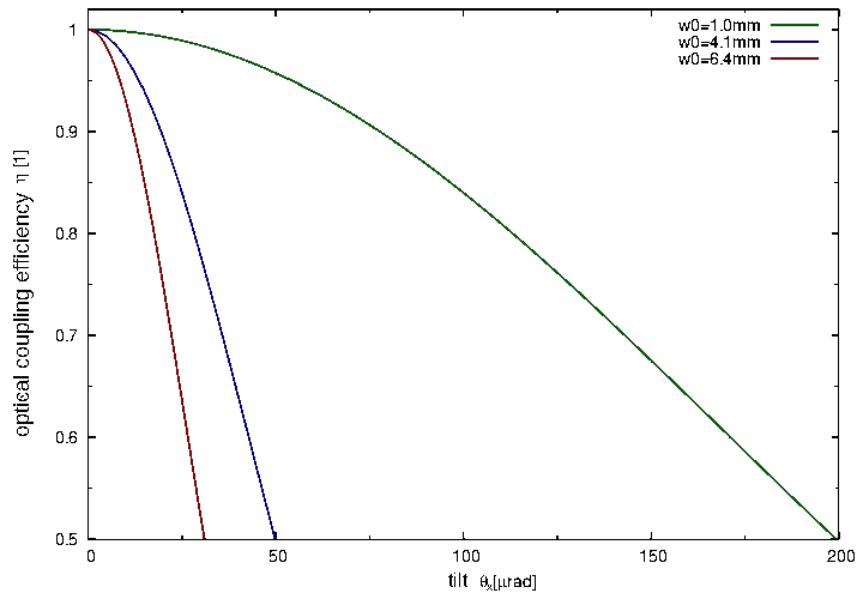
Figure 2.4: Coupling efficiency of a misaligned incident mode tilted by θ_x around the waist position of the ALPS-II cavities with $w_0 = 1.0\,\text{mm}$ (green), $w_0 = 4.1\,\text{mm}$ (blue) and $w_0 = 6.4\,\text{mm}$ (red).

2.4.2 Frequency coupling

To allow for the regenerated field to be resonantly enhanced by the RC its cavity length has to be controlled such that one of its resonance frequencies matches the frequency of the regenerated photons and thus the frequency of the PC. The frequency depending coupling losses between the Eigenmodes of the cavity with length L and a narrow-band input beam of frequency ν are governed by the Airy Function that represents the cavity build-up ratio between the incident light power P_{in} and the circulating power P_{circ} [17]

$$\frac{P_{circ}}{P_{in}} = \cdot \frac{T_1}{1 + R_1 R_2 - 2\sqrt{R_1 R_2}\cos(\delta)}$$

with R_1, R_2 the power reflectivities of the cavity mirrors, T_1 the power transmission of the input-coupling mirror respectively and $\delta = 4\pi\delta\nu L/c$, where c is the speed of light.

For the ALPS-II cavities, the frequency dependence of the resonance curves has been calculated and compared to an ideally matched one. The results that have been found according to the different stages of the ALPS-II experiment are shown in figs. 2.5 and 2.6 for PC and RC.
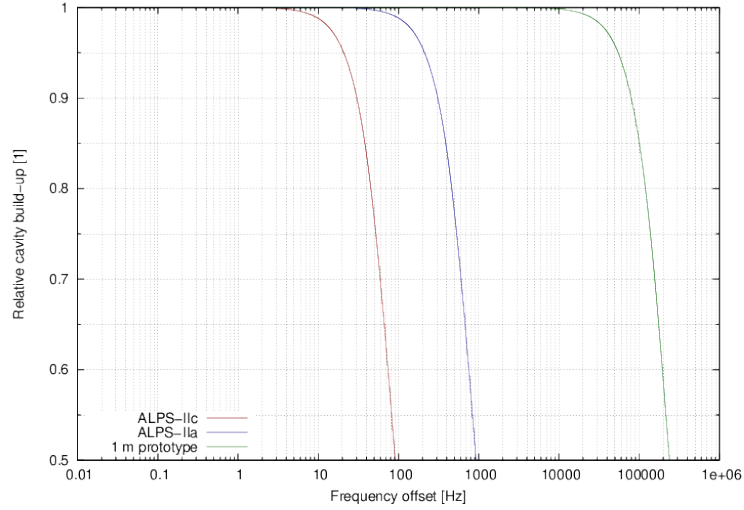
Figure 2.5: Frequency-depending cavity build-up relative to an ideally matched resonance for the ALPS-II PC in the 1 m prototype, ALPS-IIa and ALPS-IIc.
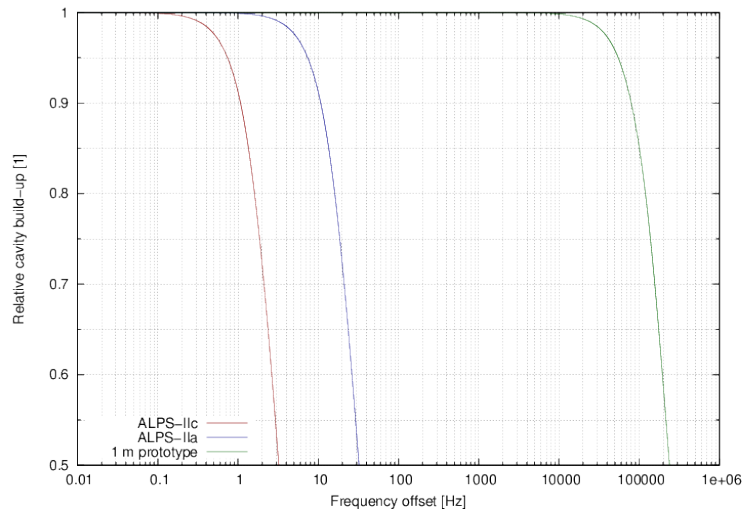
Figure 2.6: Frequency-depending cavity build-up relative to an ideally matched resonance for the ALPS-II RC in the 1 m prototype, ALPS-IIa and ALPS-IIc.

Chapter 3

Experimental methods

3.1 Central breadboard

In section 2.4 it was argued that high spatial overlap of 95 % between the optical modes of the PC and RC can only be achieved when the tilt angle between these modes does not exceed 5 µrad for ALPS-IIc and 9 µrad for ALPS-IIa. This implies a demand for precisely tuning the alignment of the planar cavity mirror surface to make them parallel and also to ensure high stability of this alignment. The approach to solve these alignment issues for ALPS-II is to fix the planar end-mirror substrates to a rigid plate, the central breadboard (CBB).

To keep alignment drifts at a minimum, the substrates are directly placed on top of the CBB and clamped with adequate pressure from a metal bar. Two different demands apply to the CBB. One is to decouple tilt misalignment of the cavity end-mirrors from environmental conditions as acoustics, ambient temperature changes and heat generated by absorption in the substrates. The other demand is linked to the initial alignment of the cavity end-mirrors. While the yaw angle of the substrates on the CBB can be adjusted by carefully pushing from the back surface, the pitch angle is basically defined by the geometry of the substrates and the CBB surface. When we seek to limit coupling losses due to alignment to less than 5 % we have to keep the total misalignment smaller than

$$\Delta\theta_{95} \approx \sqrt{0.05} \cdot \Theta = \sqrt{0.05} \cdot \frac{\lambda}{\pi w_0} \tag{3.1}$$

Assuming that the yaw alignment error can be made arbitrary small by accurate adjustment and equal distribution between a static and dynamic budget for misalignment, we can deduce the tolerances presented in table 3.1.

type	1 m prototype	ALPS IIa	ALPS-IIc
static pitch	38.0 µrad	10.0 µrad	6.0 µrad
static yaw	-	-	-
dynamic pitch	19.0 µrad	5.0 µrad	3.0 µrad
dynamic yaw	19.0 µrad	5.0 µrad	3.0 µrad

Tabelle 3.1: Budget for angular misalignment of the different stages of the ALPS experiment to limit coupling losses due to alignment to 5 % of the total power.

The pitch misalignment comprises of two parameters: first, the deviation from rectangularity between footprint area and HR coated surface of the mirror substrate and second, the surface tilt of the CBB measured between both cavity end-mirror locations.

The prototypes for the CBB that have been employed in the ALPS-II experiments so far have been fabricated of a rolled ALPLAN plate made of an alloy of aluminium, magnesium and manganese. The material offers good workability and high form stability due to very low residual stresses. To provide for additional planarity of the CBB, the top surface can be milled after drilling of the screw holes that a required for fixing the optical components later. For the prototype CBB used for the 1 m experiment this has been performed by the AEI workshop in Hannover, where the top surface was completely milled and a 60 mm wide band along the main optical axis has been specially milled without break to achieve high planarity.

Due to stricter requirements for the CBB fabricated for ALPS-IIa, this board was externally machined, milled and measured by the company ZEISS. The dimension of the board is 500 mm in length (along the direction of the main optical axis) and 350 mm in width for the basic version used in the 1 m prototype experiment. The ALPS-IIa version has an additional length of 10 mm on the regeneration side of the board to provide enough space for the placement of the shutter box. It also comprises of three ears that allow for a support of the board by specially designed mounts.

3.1.1 Surface map of the prototype CBB

A two-dimensional surface map of the CBB for the 1 m prototype experiment was measured using a coordinate-measurement machine (CMM). The CMM uses an inductive tactile probe and achieves a relative precision of up to $0.3\,\mu\text{m}$ for small point distances. A surface map was taken to examine the surface unevenness on different length scales. The coordinate system was aligned such that the abscissa (x-axis) was pointing into the direction of the main optical axis, the ordinate (y-axis) perpendicular to it in the horizontal plane and the z-axis was pointing to the top. The point density was $d_x = 1/25\,\text{mm}^{-1}$ in x-direction and $d_y = 1/17.5\,\text{mm}^{-1}$ in y-direction over the whole board. To better resolve the surface contour on smaller scales a 45 mm wide band along the x-axis was measured with an increased point density of $d_x = 1/2\,\text{mm}^{-1}$ and $d_y = 1/10\,\text{mm}^{-1}$.

The contour plots of the prototype CBB before and after milling are shown in fig. 3.1 to 3.3. In fig. 3.3, the zone with increased point density was chosen to lie within the area which was specially milled as described above.

3.2 Suppressing frequency and alignment fluctuations

To achieve the high requirements on the optical overlap of the cavity modes with the incident beams described in 2.4 active frequency and alignment control are required.

3.2.1 Pound-Drever-Hall sensing and frequency control

To keep an axial mode of an optical cavity resonant to an incident laser light field, the relative frequency changes between incoming field and resonant mode have to be measured. A well established method for sensing the relative frequency difference $\delta\nu$ is the Pound-Drever-Hall readout.

It uses phase-modulation to imprint sideband frequencies on the incident electro-magnetic field, which are anti-symmetric around the carrier frequency. In reflection of the cavity a beat pattern between the carrier light and the sidebands is detected by a photodetector. The signal on the detector is coherently demodulated with the RF phase-modulation term to obtain the so-called error signal. In a typical scenario for the use of the PDH technique,

Figure 3.1: CMM measurement of the top surface of the ALPLAN bread-board for the 1 m prototype before milling.

Figure 3.2: CMM measurement with increased point density of a selected band of the top surface of the ALPLAN breadboard for the 1 m prototype before milling.
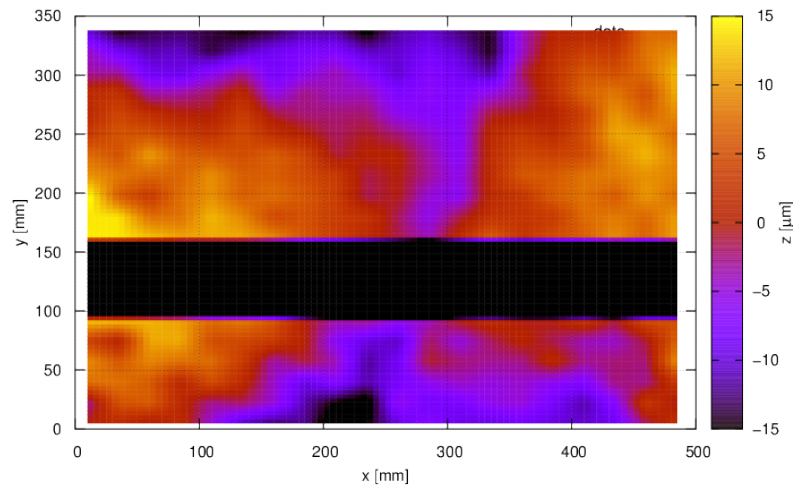
Figure 3.3: CMM measurement of the top surface of the ALPLAN breadboard for the 1 m prototype after milling.

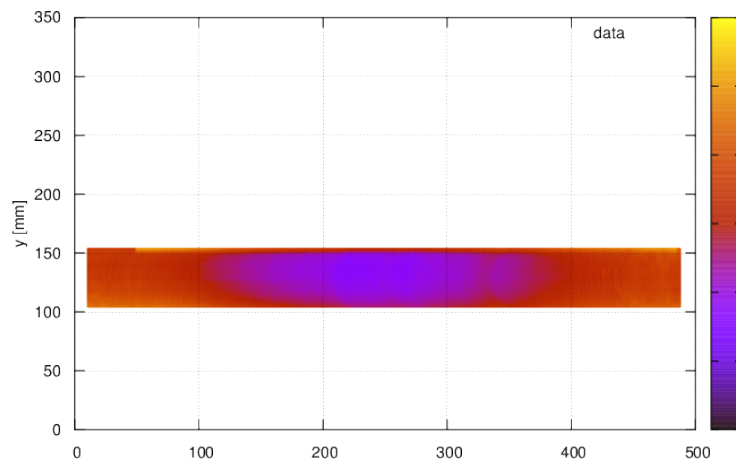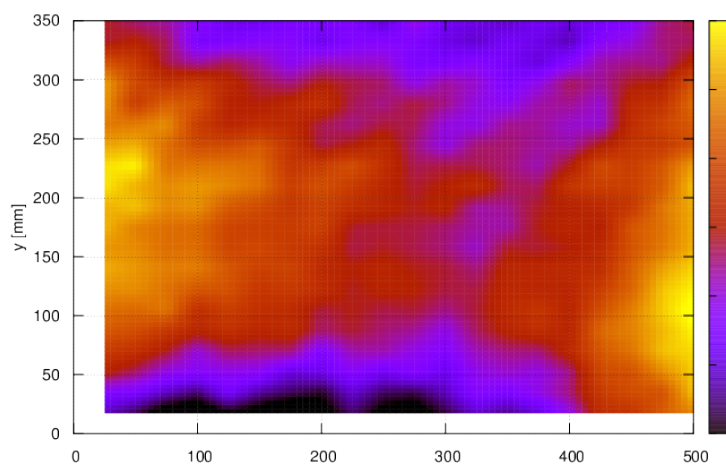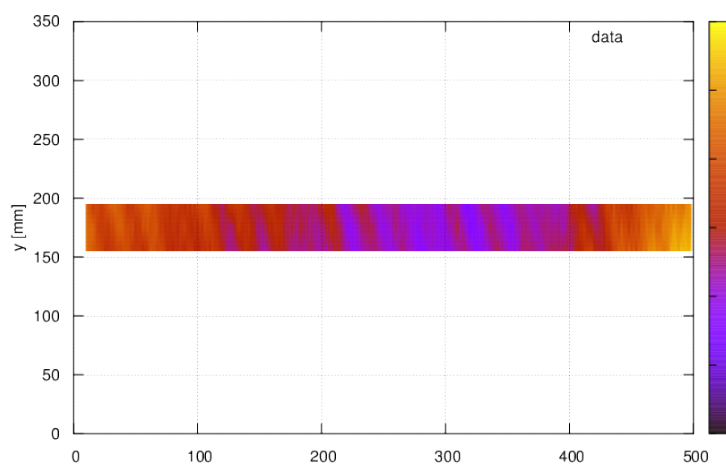
Figure 3.4: CMM measurement with increased point density of a selected band of the top surface of the ALPLAN breadboard for the 1 m prototype after milling.

the RF modulation frequency is well above the cavity linewidth $\Delta\nu_{\text{FWHM}}$. Then the error signal for a cavity near resonance will be

$$s_{\text{ES}} \propto \sqrt{P_{\text{C}} P_{\text{SB}}} \frac{\delta\nu}{\Delta\nu_{\text{FWHM}}}$$

with P_{C} the electro-magnetic power in the carrier and and P_{SB} in each of the two first-order sidebands.

A typical application of the PDH sensing is to establish a frequency control to either track the laser frequency fluctuations by changing the cavity length or to follow frequency changes of the resonant cavity mode by actuating the laser frequency. In these settings either a PZT mirror changing the cavity length or a fast frequency actuator for the laser frequency such as a PZT device stressing the laser crystal are typically employed in the stabilization. The error signal is then processed with an adequate gain and filter function and fed back to the actuator efficiently suppressing relative frequency fluctuations.

3.2.2 Differential wave-front sensing and alignment control

The differential wave-front sensing technique relies on the principle of PDH sensing but in contrast uses the sensing of higher-order modes with a multi-element split photo-diode. The misalignment of the cavity mode towards the incident beam increases the fraction of circulating power that resonates in higher-order modes. Employing an appropriately designed photodetector, e.g. a four-quadrant photo-diode (QPD), the beat signal of the incident light with the resonating modes can be detected and coherently demodulated to derive the alignment signal associated with the respective quadrant.

The resulting signal becomes a valid measure for the alignment when the roundtrip phase in the cavity $\Delta\phi = 0$, which can be achieved by stabilizing the laser frequency to a resonance frequency of the resonator using the PDH scheme. In this case, the required error signal for the frequency stabilization loop can easily be acquired by the same photodetector using a sum signal over all elements and demodulating them in the normal manner.

In a practical application, a QPD is centred on the beam axis of the cavity mode in reflection such that its gap lines are oriented to the sagittal and tangential plane. By subtracting the signals of opposing elements and demodulating the difference coherently with the local oscillator, information

about the horizontal and vertical misalignment are acquired.

Depending on the Gouy phase difference ψ of the detector to the waist position of the cavity mode different projections of the epsilon parameter can be analysed. For $\psi = 0$, the demodulated signal will be determined by a transversal shift between incident beam and resonator mode, for $\psi = \pi/2$ it will represent the tilt. For small alignment mismatches $|\epsilon| \ll 1$ the signals are proportional to the corresponding projection of the ϵ parameter.

To suppress relative alignment fluctuations in all degrees of freedom, four control loops with appropriate alignment actuators have to be established. A set of two vertically and horizontally steerable mirrors is suitable for actuating the alignment of the incident beam. Each mirror is able to manipulate the quadrature component of the epsilon beam parameter corresponding to its Gouy phase position. For efficient alignment control, the actuators are ideally separated by $|\psi_{\mathrm{A}} - \psi_{\mathrm{B}}| \approx \pi/2$.

3.2.3   Detector characterization

In the frequency and alignment stabilization loops, QPDs have been employed for the detection of RF signals and power levels of optical beams at wavelengths of 532 nm and 1064 nm. The QPD sensor device consists of a photo-detector, read-out electronic with trans-impedance amplifier and a post that allows to mount the photodiode under a 45° angle. This 45° mounting is used to overcome some problems with the original design that had foreseen to align the quadrant gap lines diagonal to the horizontal and vertical axes. This setup was therefore believed to promote undesirable couplings between the vertical and horizontal signals for off-center beams.

The photo-detector is an InGaAs PIN photodiode with a circular active area that is split in four quadrants. The diameter of the active area is 2520 µm with a gap size of 24 µm between the elements. The photo-diode has a response of about 0.18 A/W [12] at 1064 nm. Together with the trans-impedance amplifier that features a $R = 4$ kΩ feedback resistor, this results in a voltage response of 720 V/W. These signals are then spectrally filtered to output a DC signal and an AC-coupled signal with a tunable resonance frequency that is used to efficiently extract signals at the modulation frequency that is employed in PDH sensing and DWS.

To characterize the response to modulation of the optical power at different frequencies, a transfer function of the signal of a single QPD element

has been measured. A transfer function

3.2.4 Alignment signals

The signals from the QPD are further processed in a dedicated analogue electronic device. The DC signals are added and subtracted such that a sum signal

$$U_\Sigma = U_A + U_B + U_C + U_D$$

is calculated, which is useful for the measurement of the total light power on the QPD. Furthermore, two difference signals are generated, the horizontal

$$U_x = U_B + U_C - U_A - U_D$$

and the the vertical one

$$U_y = U_A + U_B - U_C - U_D.$$

These can be employed to measure the alignment of the optical beam to the sensor. The calibration of these alignment signal is described in 3.2.5. They can also be used to further calibrate the AC signals from the QPD. These are demodulated by frequency mixing with the local oscillator that feeds the sideband modulation to the laser beam. The demodulated signals are then processed in the same way to calculate the sum δU_Σ as well as horizontal and vertical difference signals δU_x and δU_y.

3.2.5 Calculating the QPD difference signal response

We assume that the beam diameter $2w$ on the detector is much smaller than the diameter of the total (circular) detector area but much larger than the gap size between the detector elements. If the beam is centred on the detector the total beam power is split equally among all four segments. We now consider two adjacent elements A and B which together detect half the total beam power of the centred beam and two opposing elements C and D which see the same light power. The situation changes when the beam center is moved by a distance Δx perpendicular to the split axis of the half circles.

The power on the half circle AB is now given by [13]

$$P_{BC}(\Delta x) = \frac{P_\Sigma}{2} \cdot \mathrm{erf}\left(\frac{\sqrt{2}\Delta x}{w}\right) \tag{3.2}$$

with the Gaussian error function $\mathrm{erf}(z)$, which is defined as

$$\mathrm{erf}(z) = \frac{2}{\pi} \int_0^z e^{-t^2} dt. \tag{3.3}$$

The power on the other half circle CD is changed just the same way with opposite sign for the error function. Thus, the expression for the difference signals P_x result to

$$\frac{P_x}{P_\Sigma} = \mathrm{erf}\left(\frac{\sqrt{2}\Delta x}{w}\right) \tag{3.4}$$

For small off-center distances Δx the error function can be simplified to the lowest order term of its Taylor expansion:

$$\mathrm{erf}(z) \approx \frac{2}{\sqrt{\pi}}z + \mathcal{O}(z^3) \tag{3.5}$$

Then, the distance Δx in units of the waist size w can be easily accessed from the sum and difference signals:

$$\frac{\Delta x}{w} \approx \frac{1}{\pi}\frac{P_x}{P_\Sigma} \tag{3.6}$$

3.3 Calibrating the automatic alignment error signals

The signals that are employed for the alignment loop channels by the QPD sensors also allow to quantitatively analyse the free-running and the residual pointing noise. In order to derive the motion of the incident beams relative to the cavity modes in units of radians and meters, the signals have to be calibrated correctly.

For calibration of the error signals of the alignment channels in terms of beam parameter changes, two different measurements can be used: calibrating the signal using the actuator or using the sensor. The actuator calibration relies on specifications for the induced tilt per voltage made by the manufacturer of the three-axes PZT devices. If a modulation amplitude

is applied to the actuator and the corresponding signal amplitude on the QPD sensor is measured, the beam parameter changes can be calibrated.

Another approach is to calculate the sensitivity of the QPD difference signals for the movement of a Gaussian beam profile around the center of the sensor with a given sum signal and beam diameter. These signals can be related to beam parameter changes and measured at the same time as the demodulated signals.

3.3.1 Actuator characterization

While the DWS method is capable of detecting alignment fluctuation, an automatic alignment system also requires adequate actuators to feed back to the optical system. The ALPS-II automatic alignment system is designed to steer the incident beams to the optical cavity to track the cavity mode.

For ALPS-II, two deflection mirrors with two tilt axes each are used to cover the required four degrees of freedom to actuate the alignment for each cavity (see 3.2.2). Commercial tilt actuator units from manufacturer Physik-instrumente are employed that consist of three piezo-electric transducers in a triangular configuration. To translate the control signals for horizontal and vertical movement that are generated by the automatic alignment loops to the triangular basis of the actuators a dedicated high-voltage driver is used that was developed by Gerhard Heinzel [16].

Each alignment actuator has a tilt range of 1200 µrad in vertical and horizontal direction. To test the actuator response to RF signals, a transfer function has been measured for a complete actuator unit including the driver from input signal to tilt angle. The measurement was done using a laser beam and a QPD detector for three different modulation amplitudes. A large signal corresponding to 30 % of the full range, a medium signal with 3 % and a small signal equivalent to 0.3 % of the full range in stationary application. Fig. 3.6 shows that in all cases an actuator bandwidth of about 700 Hz is achieved, but for larger modulation amplitudes phase loss sets in earlier.

3.3.2 Placement of the alignment actuators

Laser beam alignment to an optical cavity Eigenmode requires four degrees of freedom. For the automatic alignment system employed in the ALPS-II experiments, these are split into two actuators with one horizontal and one

vertical tilt axis each.

The placement of the alignment actuators plays an important role in the design of an automatic alignment system. The Gouy phase of the beam at the actuator position determines the phase of the changes to the ϵ parameter of the beam with respect to the cavity mode.

Maximum range and mitigation of cross-talk between the alignment channels can be achieved when both actuators are orthogonal in their Gouy phase and therefore independently manipulate the ϵ beam parameter.

While not necessarily required, in experimental application it has also been found beneficial to attribute one of the channels close to a pure tilt around the cavity mode waist and the other with almost only transversal movement of the beam center. This helps to interpret signals in a comprehensible and graphic manner.

However, the placement of the actuator in the alignment path of the cavity is also restricted by other optical components, e.g. deflection mirrors and mode-matching lenses. Furthermore, a Gouy phase of $\Psi = 90°$ or $\Psi = -90°$ as described above is not exactly accessible because these values represent the asymptotic description of the infinite far-field of an optical waist.

The placement of the alignment actuators on the beam path upstream of the ALPS-II cavities tries to mitigate these difficulties with reasonable trade-offs. The mode-matching of the ALPS-II 1 m long prototype cavity is depicted in fig. 3.7.

3.3.3   Determining the actuator Gouy phase position

In the previous section we have learned about a suitable setup for the placement of the automatic alignment actuators. Nevertheless, for a focussed beam the Gouy phase can rapidly change around the beam waist position. Thus, in the experimental setup it is often difficult to exactly determine the correct placement of the actuator simply by measuring its position along the beam axis. Therefore, a robust method has to be employed that allows to retrieve information about the actuator Gouy phase Ψ_{mod}.

This can be achieved by investigating the characteristic curve of the signal amplitude on the QPD sensors along the beam axis in the detection path. By applying a periodic modulation signal on the vertical or horizontal channel of one of the actuators and moving the QPD detector along the optical axis close to where the beam is going through a focus, the evolution of

the difference signal amplitude can be analysed and the results matched with predictions for different Gouy phase positions of the actuator. If the recorded data is fit to simulated curves, this technique can yield results that will overcome possible uncertainties, which other methods relying on direct geometric measurements of the actuator position face, and which are less prone to systematic errors.

A beneficial aspect of the procedure described here is, that the results can be fitted even without knowledge of the applied modulation amplitude and the alignment signal calibration. Therefore, the modulation amplitude will be tuned to a suitable strength that yields descent signals on the detector that can be recorded in arbitrary units. Also, in an ideal situation, where all imaging elements are non-cylindrical, the results are expected to be identical for vertical and horizontal beam modulation and sensing.

At first, the effect of the alignment actuator on the ϵ beam parameter will be calculated. Therefore, we consider an actuator tilting a deflection mirror around the reflection point of a Gaussian beam. If the Gouy phase of the beam at the mirror is Ψ_{mod} with respect to a beam waist w_0 and the mirror is tilted by an angle α then ϵ is composed by a transversal shift of the beam center in the waist and the angular misalignment, resulting in

$$\begin{aligned}
\epsilon_\alpha(\Psi_{\text{mod}}) &= \frac{\pi w_0^2}{\lambda} \cdot \tan(\Psi_{\text{mod}}) \cdot \sin(\alpha) + i\frac{\alpha}{\Theta_D} \\
&\approx \frac{\alpha}{\Theta_D} \cdot (\tan(\Psi_{\text{mod}}) + i) \qquad \text{for } \alpha \ll 1
\end{aligned} \tag{3.7}$$

where $\Theta_D = \frac{\lambda}{\pi w_0^2}$ is the half divergence angle of the Gaussian beam. In the next step, we model the transversal movement of the beam at a certain Gouy phase position. This is what is sensed by the DC signal of the QPD. Since the ϵ parameter is preserved [25], the Gouy phase can refer to the same beam waist as above or to a different one. The transversal movement at Gouy phase Ψ is

$$\begin{aligned}
\Delta x_\Psi(\epsilon) &= \Re(\epsilon) \cdot w_0 + \sin(\Im(\epsilon) \cdot \Theta_D) \cdot \frac{\pi w_0^2}{\lambda} \cdot \tan(\Psi)) \\
&\approx w_0(\Re(\epsilon) + \Im(\epsilon) \cdot \tan(\Psi)) \qquad \text{for } \alpha \ll 1
\end{aligned} \tag{3.8}$$

Using (3.7) and 3.8 we can simulate the response of the optical beam to the alignment actuator and apply (3.6) to calculate the QPD response. We

demonstrate the simulation of the difference signals for the QPDs in a beam path with a $63\,\mu m$ waist similar to the beam path for the DWS at the $1\,m$ prototype setup.

In fig. 3.8a the beam waist and Gouy phase in the detection path of the PC are plotted. For different placements of an actuator that tilts the optical axis with an amplitude $\alpha_{mod}/\Theta_D = 0.1$, we can see in (b) how the beam center is transversally shifted. Part (c) displays the corresponding signal amplitude on a QPD sensor that is positioned at a specific position along the beam axis. Note, that for the position with maximum signal amplitude the Gouy phases of the actuator and sensor differ approximately by 90°. The small discrepancies are explained by the slope of the beam diameter around the peak location.

3.4   General ALPS-II layout

The planned layout of the ALPS-IIa/c stages is sketched in fig. 3.9.

A high-power single-mode single-frequency infrared laser amplifier with an output power of $35\,W$ at $1064\,nm$ is used as a light source for the ALPS-II experiment. For the operation of frequency and alignment control, also the ability for frequency modulation and a permanent high TEM_{00} content are expedient. This type of laser amplifiers was already successfully employed to pump the SHG for the ALPS-I experiment and the $200\,W$ high-power oscillator of the LIGO second generation gravitational wave detectors.

In the ALPS-II optical setup the laser light is fed through an Faraday isolator to avoid back reflections to the laser amplifier and an electro-optical modulator (EOM) imprints phase modulation sidebands with a modulation frequency of $\Omega_1 = 2.5\,MHz$ for PDH and DWS onto the beam.

Two lenses and two mirrors which can be steered by a triangular configuration of PZTs are used to match the laser beam to the Eigenmode of the PC. A portion of the light reflected from the cavity is transmitted through an alignment mirror and split by a balanced power beam splitter. Both beams are imaged by a lens and detected using a QPD. The position of the QPDs and the imaging lenses are shifted such that ideally the beam on one detector is close to a Guoy phase difference of $\phi_A = 0$ and $\phi_B = \pi/2$ on the other. These detectors provide the signals required for obtaining the PDH and DWS error signals. The correction signals for the PDH lock of the laser

to the PC are amplified by a high-voltage driver and fed back to the laser frequency via a PZT on the laser crystal. The automatic alignment control signals are translated by a driver electronic to high-voltage signals for the triangular PZT configurations of the steering mirrors.

The PC is composed of the incoupling mirror PIC with a curvature radius of $r_{\mathrm{ROC}} = -250\,\mathrm{m}$ and a power transmission of $T = 750\,\mathrm{ppm}$. It is mounted to a triangular PZT configuration for fast manipulation of the PC mode position. The PZT formation itself is attached to a steerable mount with step motors for vertical and horizontal tilt to cope with larger tilt angles for a rough alignment of the PC mode.

The planar mirror CBS1a has a transmission of $T = 11\,\mathrm{ppm}$ and is part of the CBB setup. All mirror substrates on the CBB are rigidly fixed to the board by clamping. The deflection mirror CBS1b directly behind the PC has a transmission of $10\,\%$ to allow for verifying the mutual alignment of PC and RC. The main component of the 1.8 W transmitted by the PC is deflected to be matched to the SHG, which consists of a $3 \times 3 \times 10\,\mathrm{mm}$ KTP crystal to provide an auxiliary low-power beam at 532 nm used for the frequency and alignment stabilization of the RC. Upstream of the crystal, a small fraction of the beam is diverted to another photodetector QPD3 which tracks lateral movement of the PC mode.

Downstream of the SHG a dichroic mirror sends the residual 1064 nm pump power to a beam dump outside the vacuum tank. The green beam also leaves the vacuum tank via deflection mirror MZ1, where it is frequency shifted via an acousto-optical modulator (AOM) in double-pass configuration and phase-modulated by another EOM which has a modulation frequency of $\Omega_2 = 3.5\,\mathrm{MHz}$.

The green beam is then, similar to the setup in front of the PC, matched by two lenses and two steering mirrors to the RC mode. Before injection into the RC, the beam is entering the shutter box through a configuration of four angled dichroics which prevent infrared light from entering the regeneration area. The shutter box is part of the "wall"which has a remotely triggered shutter which can open or close the beam path between the cavities.

The RC consists of a flat mirror CBS2a with an infrared transmission of $T_{1064} = 25\,\mathrm{ppm}$ and green transmission of $T_{532} = 5\,\%$ and a curved mirror REM with $r_{ROC} = -250\,\mathrm{m}$ curvature radius and transmission $T_{1064} = 11\,\mathrm{ppm}$ for the infrared and $T_{532} = 1\,\%$ for the green light. Just as

the PIC mirror, REM is steerable by a triangular PZT configuration and two PZT step motors.

The green beam reflected by the RC traces back the path of the incoming beam to QPD5 and QPD6 which are used to generate appropriate error signals for frequency and alignment control of the green beam to the RC. The corresponding control loops feed back to the steering mirrors. Here again, a position-sensitive photodetector, QPD4, tracks motion of the green RC cavity mode.

The important task to make PC and RC mode collinear can be accomplished before the CBB is finally installed to the vacuum tank. In order to do so, both flat cavity end-mirrors, CBS1a and CBS2a are carefully adjusted with respect to each other and rigidly fixed to the CBB. A temporary setup interferometer between both HR coated surfaces can help to ensure that the substrates are aligned in parallel.

To laterally match both cavity axes, the PC is stabilized on resonance and the shutter is opened. Now one of the cavity end-mirrors PIC or REM is adjusted until both cavity Eigenmodes overlap well. This can be evaluated by ramping the length of the RC cavity by applying an axial modulation to the PZTs of mirror REM and monitoring the peak height of the Gaussian ground mode in the RC. The vertical and horizontal difference signals from QPD3 and QPD4 characterize the beam position permanently as far as CBS1a, CBS2a, QPD3 and QPD4 do not change their relative position. After closing the shutter, these signals remain valid. Therefore, the position of the cavity modes can be fixed in the long-term by establishing a control loop that feeds back to the tilt alignments of PIC and REM.
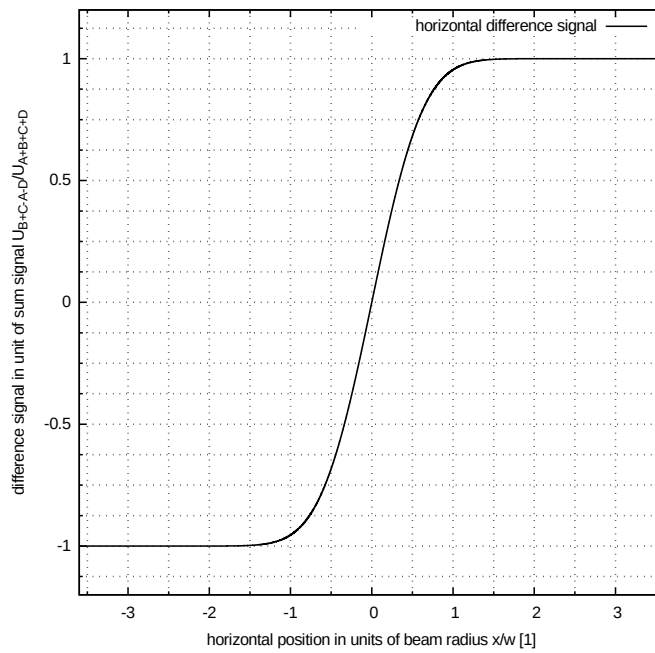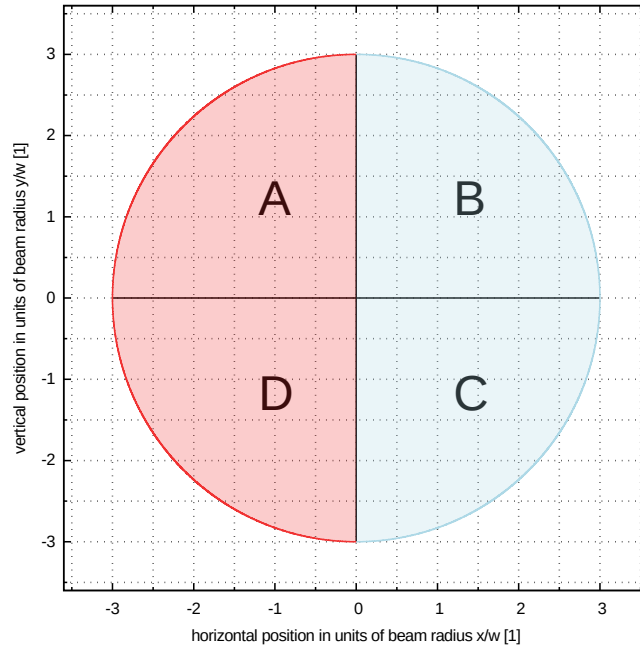
(a)

(b)

Figure 3.5: (a) Schematic sketch of a set of QPD segments. (b) Difference signal U_x in units of the sum signal U_{sum} over horizontal beam center position x in units of the beam radius w.
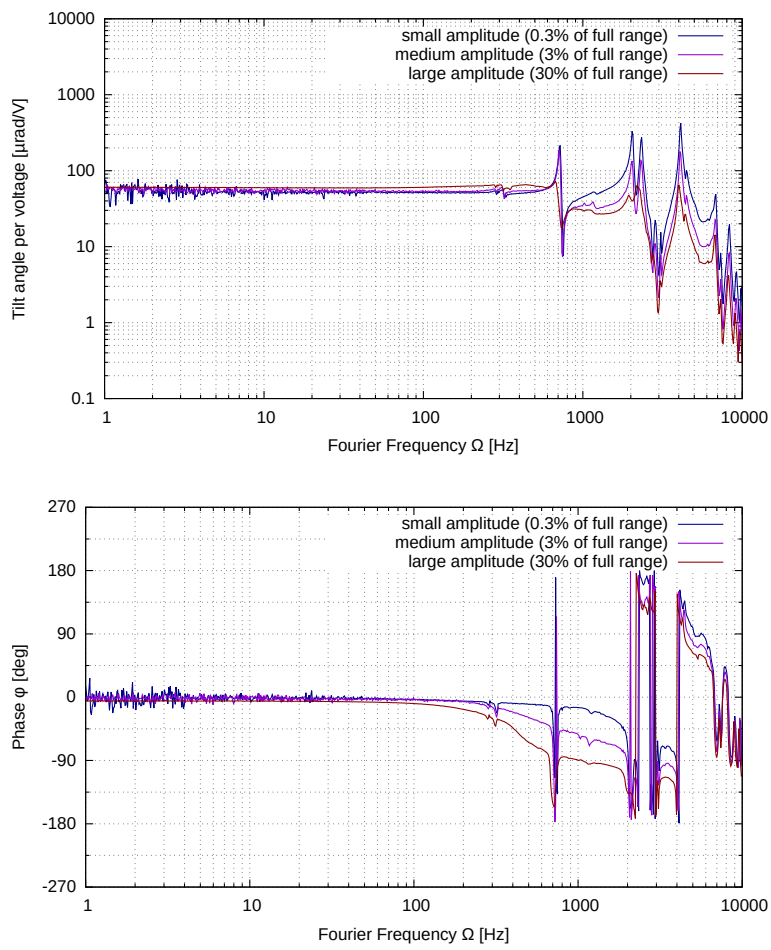
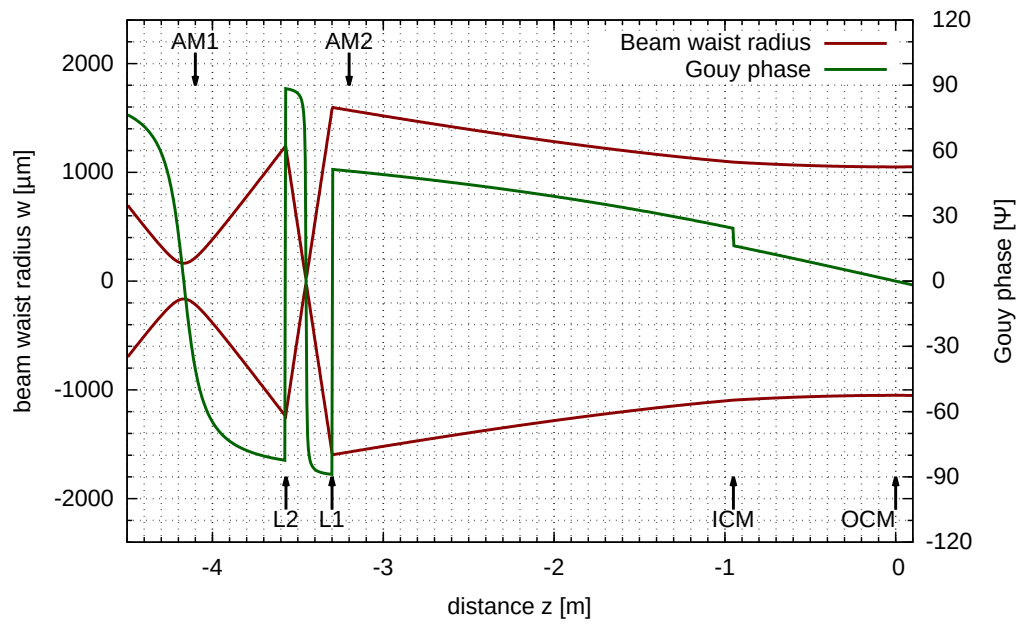Figure 3.6: Bode plot of transfer function from PZT alignment actuator including driver from input voltage to tilt angle.

Figure 3.7: Modematching of the 35 W laser beam to the 1 m long PC. The beam radius is plotted in red, the Gouy phase in green. Modematching lenses and alignment actuator positions relevant for the automatic alignment system have been included. Axial positions of components relevant for the modematching have been marked with black arrows: alignment actuator mirrors AM1 and AM2, lenses L1 and L2 with focal radii of $f_{L1} = 100$ mm and $f_{L2} = 150$ mm as well as the input coupling mirror ICM and the output coupling mirror OCM
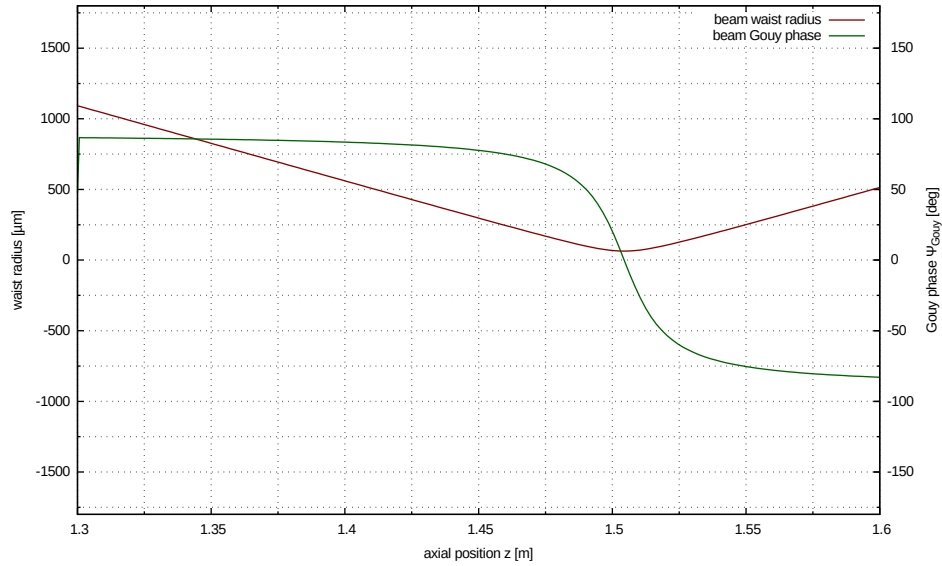
(a)
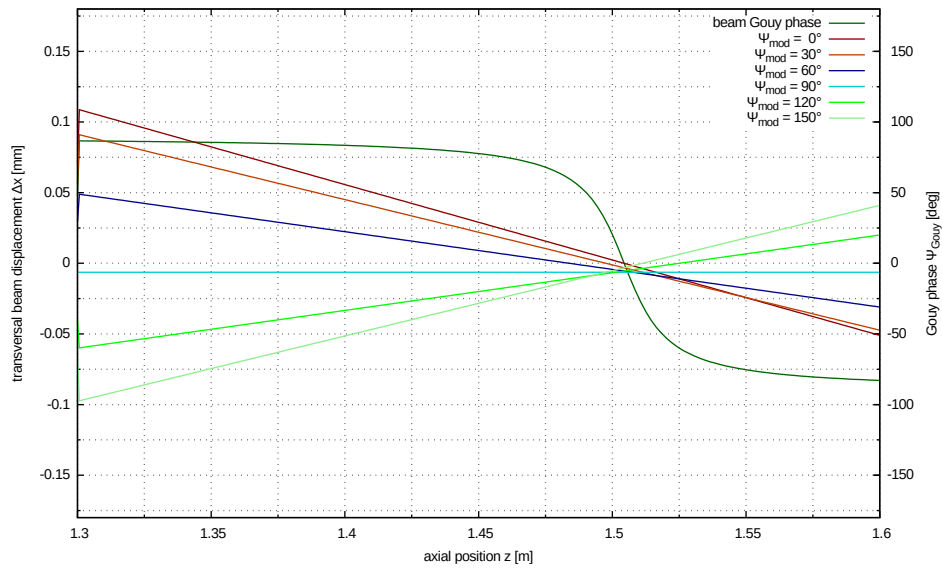
(b)
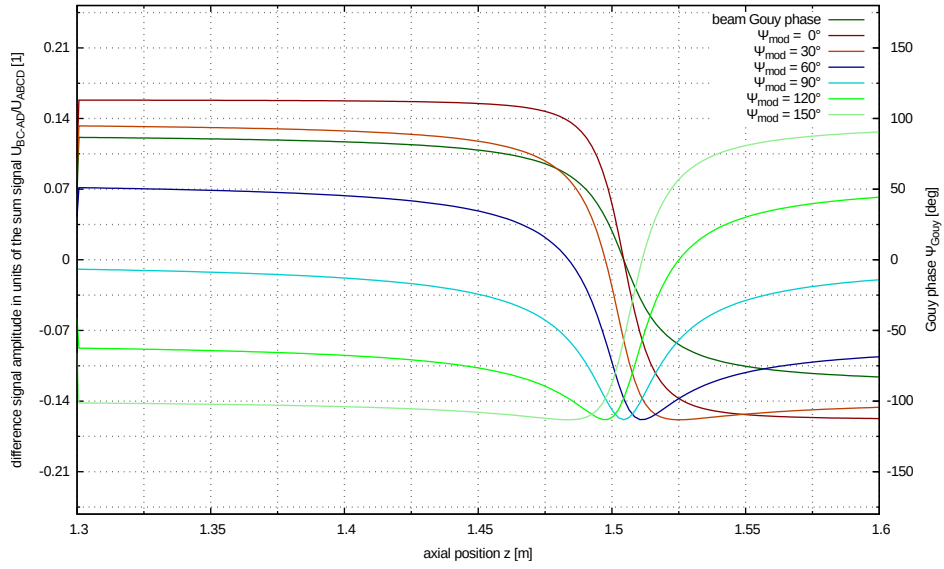
(c)

Figure 3.8: (a) Waist size and Gouy phase of the beam in the detection path for the automatic alignment sensors over distance z from the cavity waist with $w_0 = 1$mm along the optical axis. (b) Simulated transversal movement of the beam profile center for a modulation of the beam alignment by a tilt mirror located at different axial positions corresponding to a Gouy phase of Ψ_{mod} with a peak-to-peak tilt amplitude of $\alpha_{\mathrm{mod}}/\Theta_{\mathrm{D}} = 0.1$ (c) Simulated signal amplitudes for these alignment modulations for a placement of the detector at position z along the optical axis.
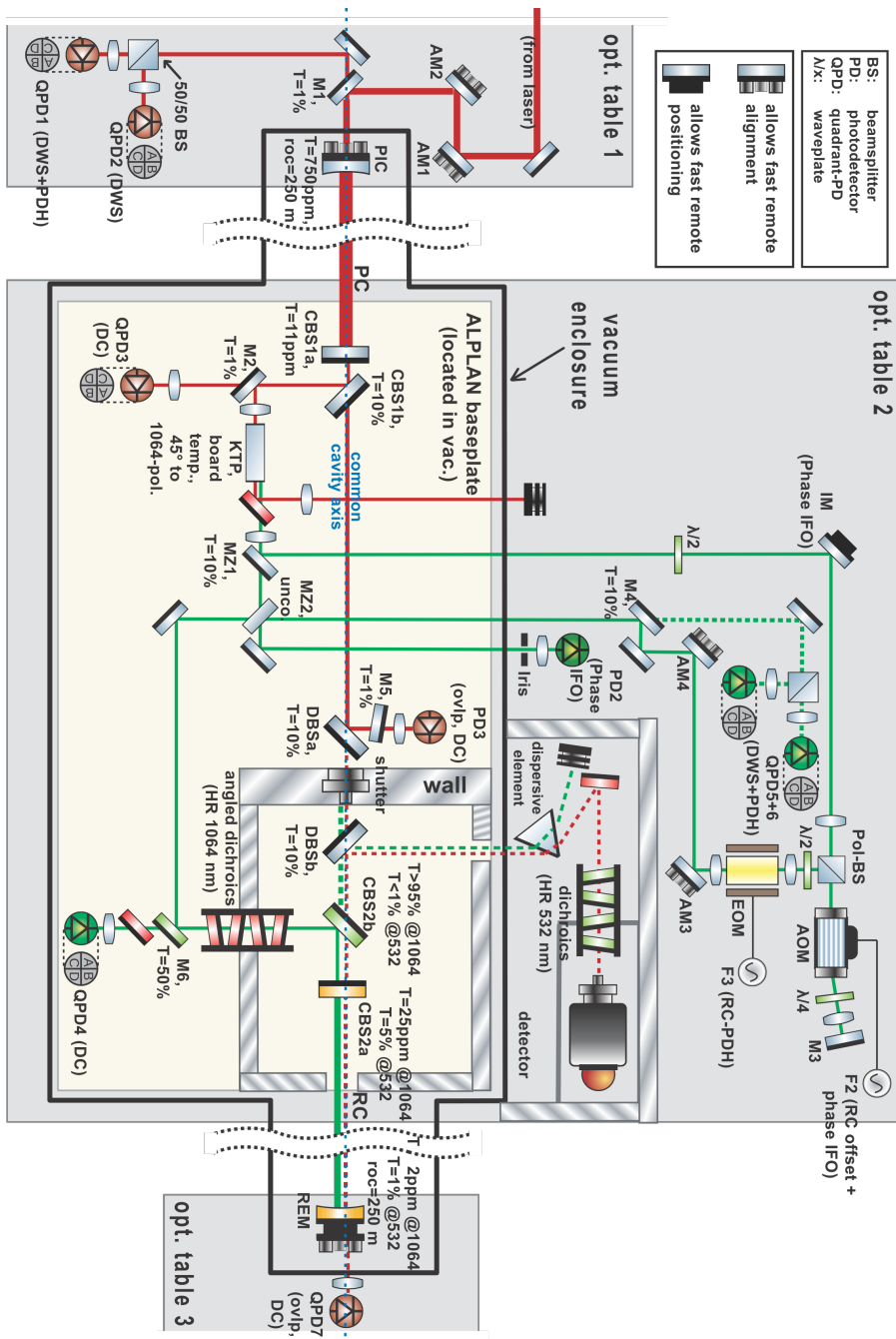
Figure 3.9: Schematic sketch of the optical layout for the ALPS-IIa/c stages. Detailed description of the setup and employed optical components is found in section 3.4

.

Chapter 4

Results of the prototype setup

The DESY in Hamburg provides large facilities and infrastructure for performing experiments with the 10 m long and 100 m long high-finesse cavities. Nevertheless, part of the development and characterization can be performed using a table-top setup, which has relaxed requirements and offers better feasibility of alignment. Therefore, an ALPS-II prototype setup of two 1 m long cavities with a finesse of $\mathcal{F} \approx 300$ was installed in a laser laboratory at the AEI. The prototype does not include a single photon detector, ambient and straylight protection as well as vacuum tubes and therefore is designed for a proof-of-concept rather than for a physics run probing the existence of WISP particles.

The basic experimental setup of the 1 m prototype is in many aspects equivalent to that of ALPS-IIa. The laser system in use is also a 35 W laser amplifier which can be suitably attenuated using a waveplate and polarizing beam-splitter. The piezo-mounted curved cavity end-mirrors are affixed to a copper base placed on a 4-axis adjustment table. The CBB is a functional prototype of the ALPS-IIa version that comes without the supports for three point bearing but instead is supported by four posts with a layer of viton rubber in between. The two free-space 1 m cavities are not enclosed in a vacuum system. To reduce airflow and air pressure fluctuations, which would induce additional frequency noise on the cavity, the beam is shielded by a beam tube with 1 in diameter. The tube covers the full distance of the cavities with a margin of only $1 - 2$ mm with respect to each of the cavity end-mirrors.

4.1 Characterization of the 1 m cavities

The PC and RC are linear cavities, which consist of a planar and a curved end-mirror. For the 1 m cavities the cavity mirrors have equal power reflectivity for infra-red light by design. With $R_1 = R_2 = 0.99$ a cavity finesse of

$$\mathcal{F} = \frac{\pi}{2\arcsin(\frac{1-\sqrt{R_1 \cdot R_2}}{2\sqrt{R_1 \cdot R_2}})} \approx 312.6$$

is expected for 1064 nm. This can be experimentally verified by determining the full-width half-maximum bandwidth $\Delta\nu$ and the free spectral range $\delta\nu_{\mathrm{FSR}}$ of the cavity. The free spectral range defining the spacing of the longitudinal cavity modes is given geometrically by

$$\delta\nu_{\mathrm{FSR}} = \frac{c}{2 \cdot L}, \tag{4.1}$$

where c is the speed of light and L the distance between the cavity mirrors. The length of the 1 m cavities is more precisely set up to be 95 cm for both, the PC and RC. Therefore, a free spectral range of $\delta\nu_{\mathrm{FSR}} \approx 157.8$ MHz is calculated. The cavity bandwidth can be extrapolated from a mode-scan of the cavity with sufficient accuracy for this case. The mode-scan is taken by linearly varying the laser frequency and simultaneously detecting the transmitted light power with a photo-detector.

For the PC a finesse $\mathcal{F}_{PC} = 288$ was determined, for the RC the measured finesse was $\mathcal{F}_{RC} = 280$ at a wavelength of 1064 nm.

4.2 Characterization of the frequency/length stabilization loop of the PC and RC

The open-loop transfer function is an important tool to quantify the ability of a feedback loop to suppress noise impacts on a controlled variable. While contributions at different parts of the loop can still introduce additional noise to the controlled variable, the gain of the curve describes the measured suppression of input signals within one round-trip.
The open-loop transfer functions of the frequency stabilization loop for the PC and of the length stabilization loop of the RC have been recorded using a network analyser. While the loop was closed, a sweep sine modulation signal
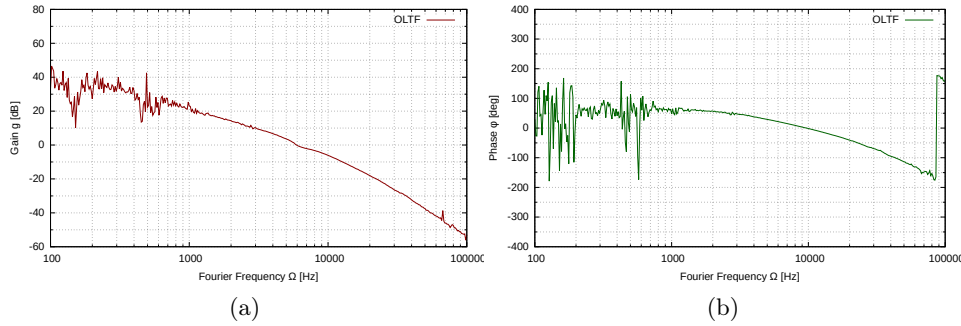
Figure 4.1: Bodeplot of the open loop transfer function of the frequency stabilization loop of the ALPS-II prototype PC.
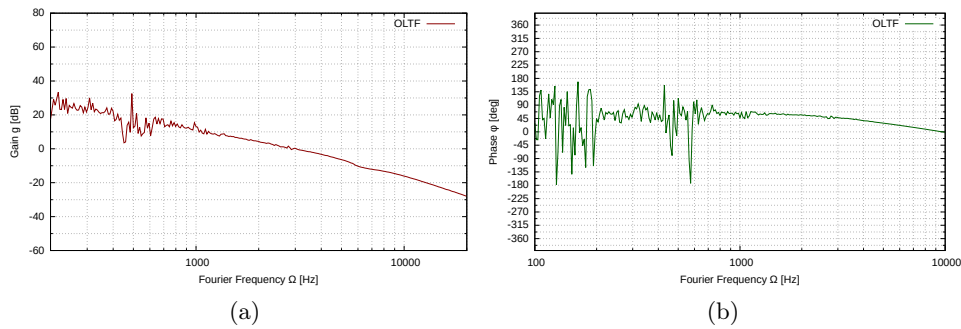
Figure 4.2: Bodeplot of the open loop transfer function of the frequency stabilization loop of the ALPS-II prototype RC.

was added to the unity-gain input adder of the servo while the quotient of the response amplitude at the output of the demodulation unit and the amplitude behind the servo input adder were measured. For these measurement, no additional integrator stages were used.

The measurement result of the open-loop transfer function of the PC frequency stabilization loop is presented in fig. 4.1. A unity gain frequency of 5.7 kHz was determined. The open-loop transfer function of the dichroic RC length stabilization was measured in the same way. The measurement result is plotted in fig. 4.2.
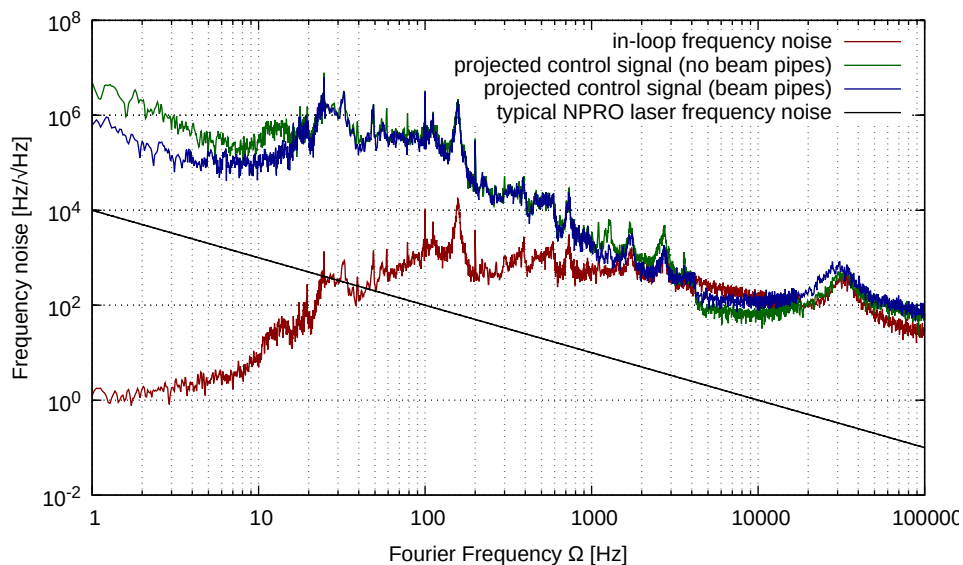
Figure 4.3: Frequency noise spectral density projected from error signal (red) and from control signal of the 1 m long PC without beam pipe (green) and with beam pipe (blue) around the cavity mode. A typical frequency noise curve of the NPRO laser is plotted as an orientation (black). The second axis of ordinate calibrates the frequency changes as length changes of the cavity.

4.3 Cavity length fluctuations

By stabilizing the laser frequency to one of the longitudinal modes of the PC, information can be acquired about relative frequency changes between laser and cavity and by this, an upper limit can be set on the free-running length fluctuations of the cavity.

An FFT spectrum of the control signal noise density was taken at the output of the PDH servo with the loop closed. This spectrum can be used to project the frequency changes beween laser and cavity. Therefore, a calibration of the control signal is performed in frequency change $\Delta\nu = 2 \cdot c \cdot \Delta L / \lambda$ by determining the control signal voltage difference related to two adjacent axial modes of the cavity. The results are presented in fig. 4.3

A typical frequency noise curve of the MOPA laser [30][5] which has also been observed for the amplified laser stage shows a frequency noise spectral density of 10 kHz/$\sqrt{\mathrm{Hz}}$ at a Fourier frequency of 1 Hz and exhibits a $1/f$ behaviour. It has been plotted in black colour.

Since the free-running cavity length noise lies well above the expected

laser noise, we can attribute the measured fluctuations almost completely to the cavity. A reduction of the free-running cavity length fluctuations for low Fourier frequencies $\Omega \leq 15$ Hz has been achieved by shielding the cavity mode from air flow with a 1 in beam pipe (see blue curve). This modification allowed for significantly longer locking times with typically one to ten minutes before the laser frequency actuator reached the end of its dynamical range.

The in-loop noise shows a suppression by three orders of magnitude at Fourier frequencies around 1 Hz. However, the real performance that an out-of-loop measurement would reveal might actually be higher.

A prediction for the ALPS-IIc cavities from these results cannot be made. Not only because of the different cavity length, but also, because seismic and acoustic excitation can be different in the HERA hall environment and air fluctuations will not occur in the evacuated ALPS-IIc cavities.

4.4 Relative intensity noise of the circulating light

The setup of the 1 m prototype experiment allows for measurements of the optical power in transmission of the PC and the RC. This value is directly linked to the circulating power inside the cavities travelling towards the out-coupling mirror. The detected power fluctuations in transmission of the locked cavities (see fig. 4.4) are caused by power noise of the in-coupled light or by changes of the coupling between incident light and cavity mode either due to relative frequency or alignment fluctuations. Also, stray light from optical surfaces and stray events caused by dust particles in air can play a role.

4.5 Characterization of the automatic alignment loops of the PC

The automatic alignment system that is employed for the ALPS cavities divides the beam control into four separate channels. In an ideal model, all of these channels would be pairwise independent. Cross-coupling between the horizontal and vertical channels of the tilt or translation loops occurs due to non-orthogonal movement of the actuators, imbalanced proportions of the detectors or deviant orientation of the actuator and detector. Cross-coupling
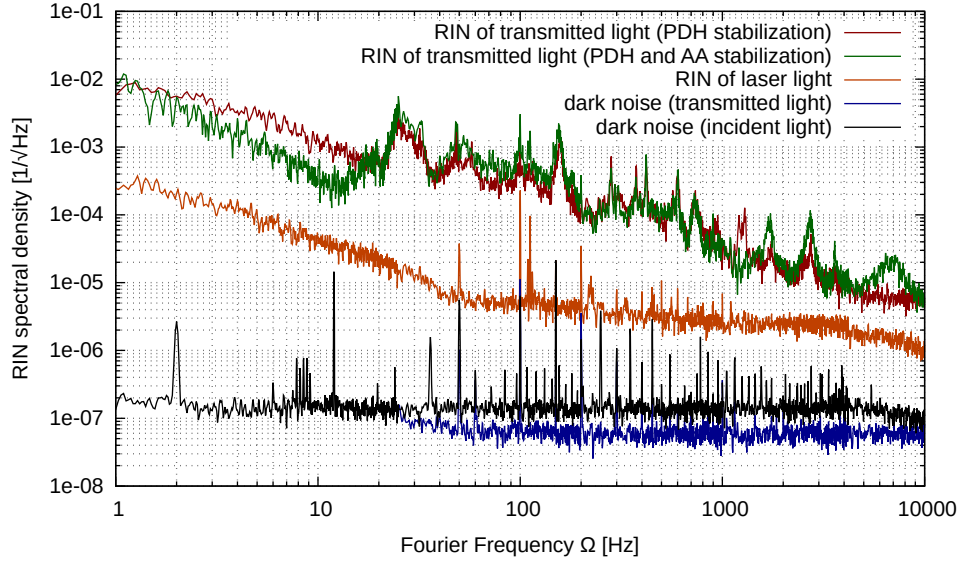
Figure 4.4: Relative intensity noise spectral density measured in transmission of the 1 m long PC with PDH stabilization enabled (red) and with PDH and AA stabilization enabled (green), relative intensity noise of the laser light incident on the cavity (orange) and dark noise of the sensor in transmission of the cavity (blue) and dark noise of the sensor for a pickup of the beam incident on the cavity (black).

between the tilt and translation channels of the horizontal or vertical loops is caused by non-orthogonal Gouy phase positions of the actuators or detectors or by a difference between the actuation and detection Gouy phase.

Moreover, if aberration in optical lenses takes place or the beam is leaving the horizontal plane, this may affect the ϵ parameter while propagating giving rise to cross-couplings. In systems, where both types of couplings exist, all channels can mutually interact. A coupling matrix depicts the parameters for all channels. In an ideal case, where no cross-coupling exists, only elements on the principal axis will have a non-zero value.

### 4.5.1 Determining the actuator Gouy phase positions for the 1 m long PC

Here, we use the beam path in reflection of the PC in the same way as it is setup for the QPD sensors employed in the automatic alignment. The reflected beam from the cavity is focused using an optical lens at position $z = 1.3$ m from the cavity mode waist with a focal length of $f = 200$ mm.

The signals are simulated in the way described in 3.3.3 and fit to the measured data. Only one actuator was modulated at a time. Signal amplitude, absolute position along the optical axis and actuator phase have been used as free parameters to the fit. Because determining the correct sign of the signal is not required and could be prone to errors, only the signal amplitude was measured for sinusoidal modulation of the actuator. The results are found in fig. 4.5.

4.5.2   Dichroic lock and power noise of the RC for 1064 nm light

For this measurement the RC length was stabilized with the dichroic lock using a green auxiliary beam for the PDH readout. The resonance frequency of the green cavity was tuned by shifting the AOM RF frequency until the infrared light transmitted by the PC become resonant at the same time as the green light. The transmitted beam was attenuated to about 10 mW to avoid pushing the RC control signal out of its range when the cavity length is thermally driven. This was observed for a 100 mW infrared beam.

The power noise spectral density for both, the red and the green light in transmission of the RC was measured. The results can be found in fig. 4.6. The measurement shows that the power noise is almost equivalent for the red and green mode for higher Fourier frequencies, which means that the frequency fluctuations for both modes are coupled. However, for lower frequencies there seems to be additional power noise, which cannot yet be explained, but might be attributed to alignment fluctuations or thermal noise. The unity gain frequency of the stabilization in this measurement was 900 Hz.
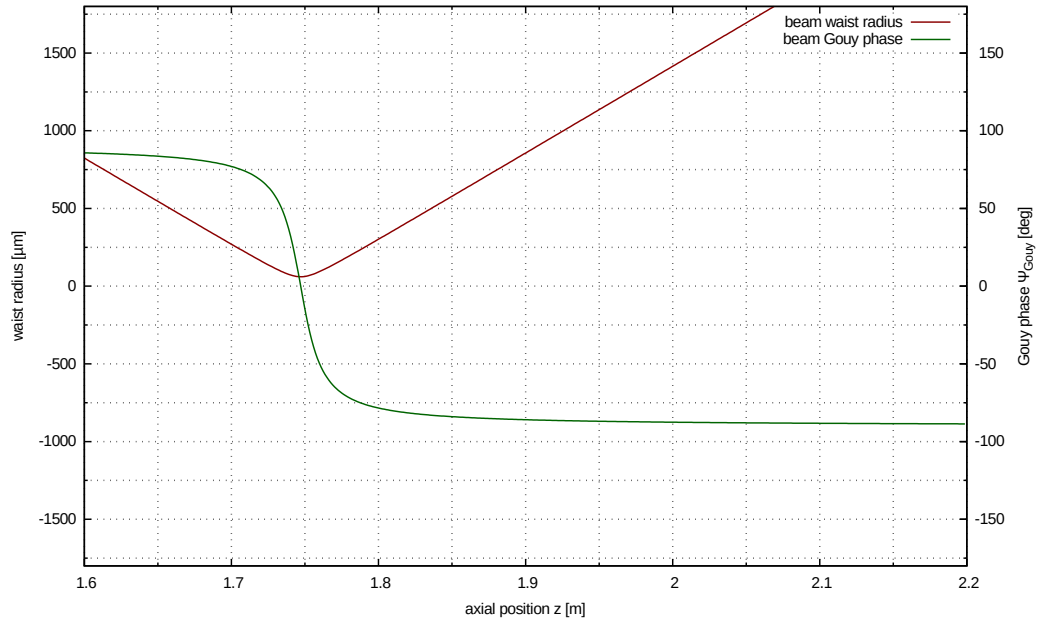
(a)
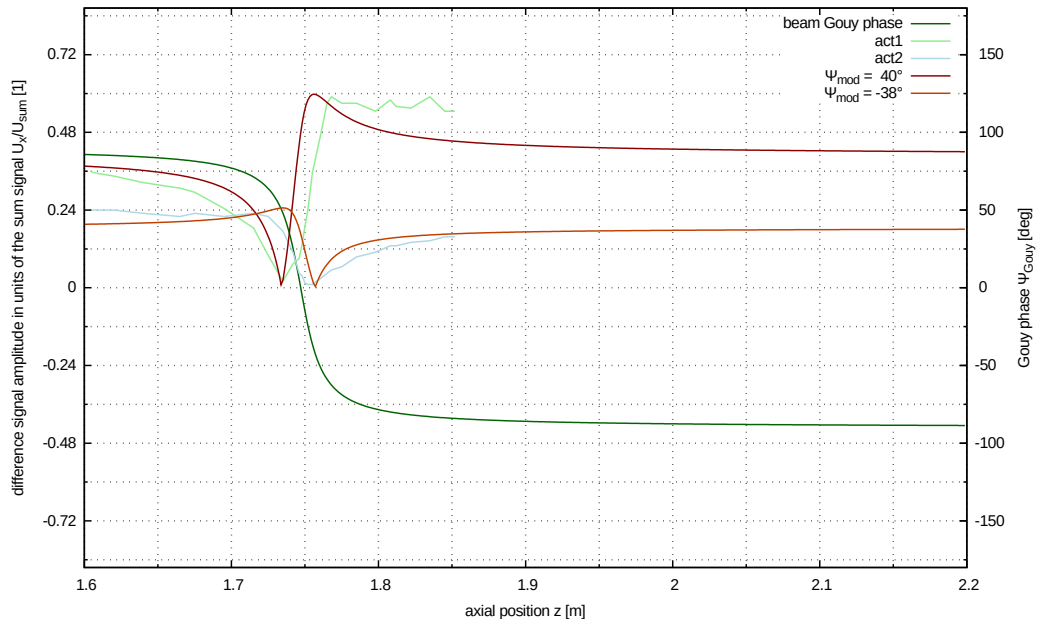
(b)

Figure 4.5: (a) Waist size and Gouy phase of the beam in the detection path for the automatic alignment sensors over distance z with respect to the cavity mode waist. (b) Measured amplitudes and fit data for the QPD difference signals.
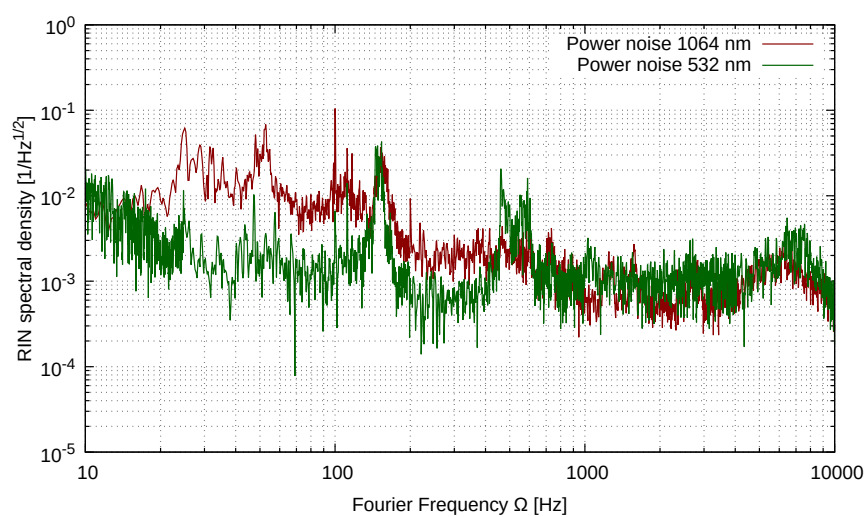
Figure 4.6: Power noise spectral density of the red and the green light with dichroic lock of the RC length.

Chapter 5

Results of the ALPS-IIa setup

ALPS-IIa is an intermediary stage of the experiment that allows for the setup of two 10 m long optical cavities in vacuum in a serial configuration. The basic idea of the setup is identical to the ALPS-IIc stage: Laser and mode-matching beam path are placed on table 1 together with the input coupling mirror of the PC, which is installed in a vacuum vessel attached to the PC beam tube. A view-port window with anti-reflective coating allows to couple the beam into the vacuum system from the laser side. The central table 2 hosts another vacuum tank for housing the CBB with the two central planar cavity mirrors. This tank is connected to the beam tubes for PC and RC. The rear end mirror of the RC is designed to be also set up in a small vacuum housing on table 3 connected to the RC beam tube.

The ALPS-IIa stage was originally planed to be operated with the same cavity mirrors that were also foreseen for the final ALPS-IIc stage, which implies that the same finesse values as for ALPS-IIc but a smaller cavity beam waist of 4 mm is expected.

5.1   Issues with the cavity finesse

When setting up the first 10 m long cavity of the ALPS-IIa setup it was realized that the finesse and transmission on resonance where far below the specifications. In [20], a cavity finesse of $\mathcal{F} \approx 1,600$ was reported and discrepancy to the expected value of $\mathcal{F} \approx 5,000$ was likely attributed to unexplained losses in the cavity of the order of 3400 ppm per round-trip. Additionally, the cavity pole frequency was found to be varying between 4 kHz and 7 kHz

[20].

Since exchanging the mirrors by others from the same fabrication run did not resolve the issue, other measures were taken to address the problems that especially arouse from the varying performance of the cavity.

In order to mitigate the high round-trip losses, it was decided to operate one cavity with 20 m length and two curved end-mirrors with a transmission of $T_1 = T_2 = 750$ ppm. Fortunately, the cavity beam waist is not affected by these changes, thus the mode-matching and alignment properties remain the same. This also means that the automatic alignment actuators and detectors can be set up in the same way as for the original setup.

Therefore, the impact of these modification on the setup and characterization that was done for this thesis work was not essential. However, temporary fluctuations of higher-order modes that flash up while the fundamental Gaussian mode is resonant might are likely to originate from the same cause. These fluctuations could probably also explain high RIN of the light transmitted by the cavity when stabilized on resonance.

Only recently, when the experiments and work on this thesis were almost finished, the reason for the finesse issues could possibly be resolved. When the curvature of two of the concave end-mirrors was send back to the manufacturer to be investigated, they were found to be far off the specifications.

The highly reflective facet of the curved PC mirror that was designed to have a curvature radius of $R_{\mathrm{ROC,front}} = -250\,\mathrm{m}$ instead showed a distorted surface after coating that clearly did not match the designed spherical geometry. Mistakes during the coating process and insufficient substrate thickness have been held responsible for the discrepancies. A set of replacement substrates has not been available in sufficient time to be included in this thesis' results.

5.2 Mode matching and placement of the alignment actuators for the ALPS-IIa 20 m cavity

The ALPS-IIa 20 m long cavity has a mode waist radius of 4 mm. The mode matching for a large collimated beam requires sufficient space and – to allow for the application of the automatic alignment system – also had to incorporate the desired placement of the PZT actuators.

Particularly the placement of the actuators is a delicate step in the setup
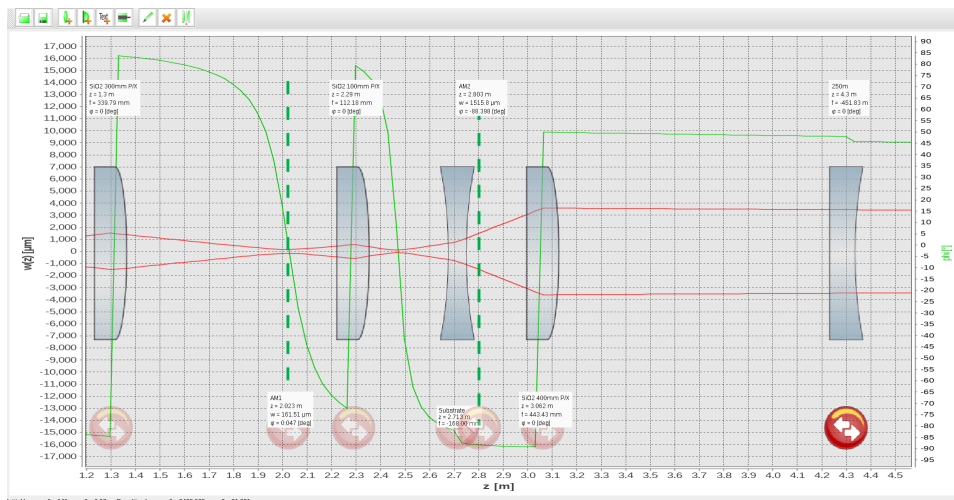
Figure 5.1: Mode matching of the 35 W laser beam to the ALPS-IIa 20 m long cavity. The beam radius is plotted in red, the Gouy phase in green on the second axis of ordinate. Optical substrates, mode matching lenses and alignment actuator positions relevant for the automatic alignment system have been included. Calculation and plot have been performed using the program JamMt [34]

because moving one of the deflection mirrors attached to the PZT actuators along the beam axis later often requires to start the setup of the downstream components all over again. The final setup that was done according to fig. 5.1 evolved in an iterative experimental process as an adequate solution for a feasible mode matching with sufficient space for the alignment actuators at a Gouy phase position $\Psi_{AM1} \approx 0°$ and $\Psi_{AM2} \approx -88°$.

If the QPD devices are placed in the detection path accordingly, this would represent a solution very close to a complete decoupling of all alignment channels. Experimentally, it turned out that couplings could be reduced but only to a certain extend. Especially for alignment mirror AM1, a coupling of up to about 40 % to the other coordinate remained.

A complete coupling matrix was measured by modulating each of the alignment actuators by an arbitrary but fixed modulation and observing the evoked signal amplitude on the different alignment sensors.

5.3 Characterization of the ALPS-IIa automatic alignment loops
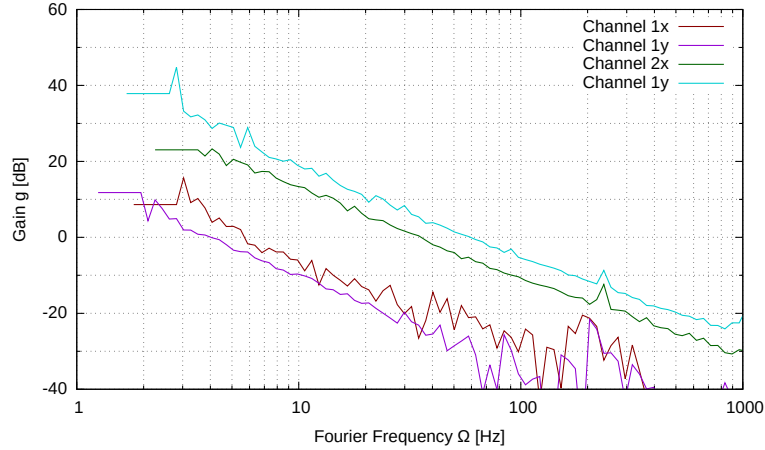
(a)
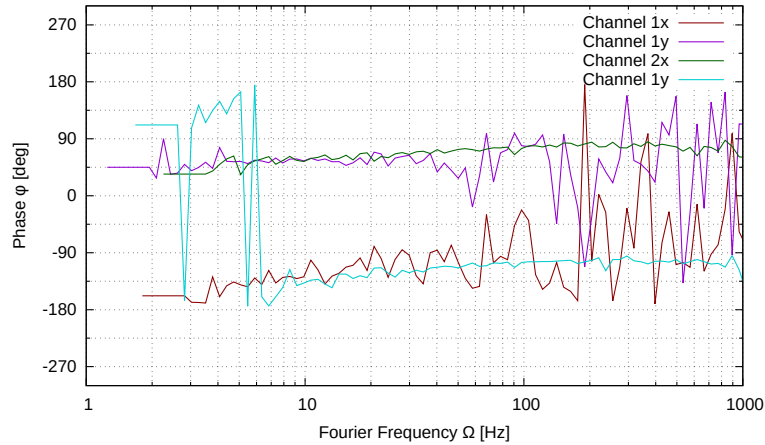
(b)

Figure 5.2: Bode plot of open loop transfer function for the automatic alignment channels of the ALPS-IIa 20 m long cavity. The unity gain frequency of channel 1x (red) is 6 Hz, the unity gain frequency of channel 1y (violet) is 4 Hz, the unity gain frequency of channel 2x (green) is 35 Hz and the unity gain frequency of channel 1y (turquoise) is 58 Hz.

The characterization of the AA loops was done by measuring transfer functions of all AA channels, when the AA was engaged. The Bode plots of these measurements can be seen in fig. 5.2. From the spectra of the error signal and control signal of each individual channel, the pointing noise

performance for the incident beam to the cavity mode was calculated. The results are displayed in fig. 5.3.
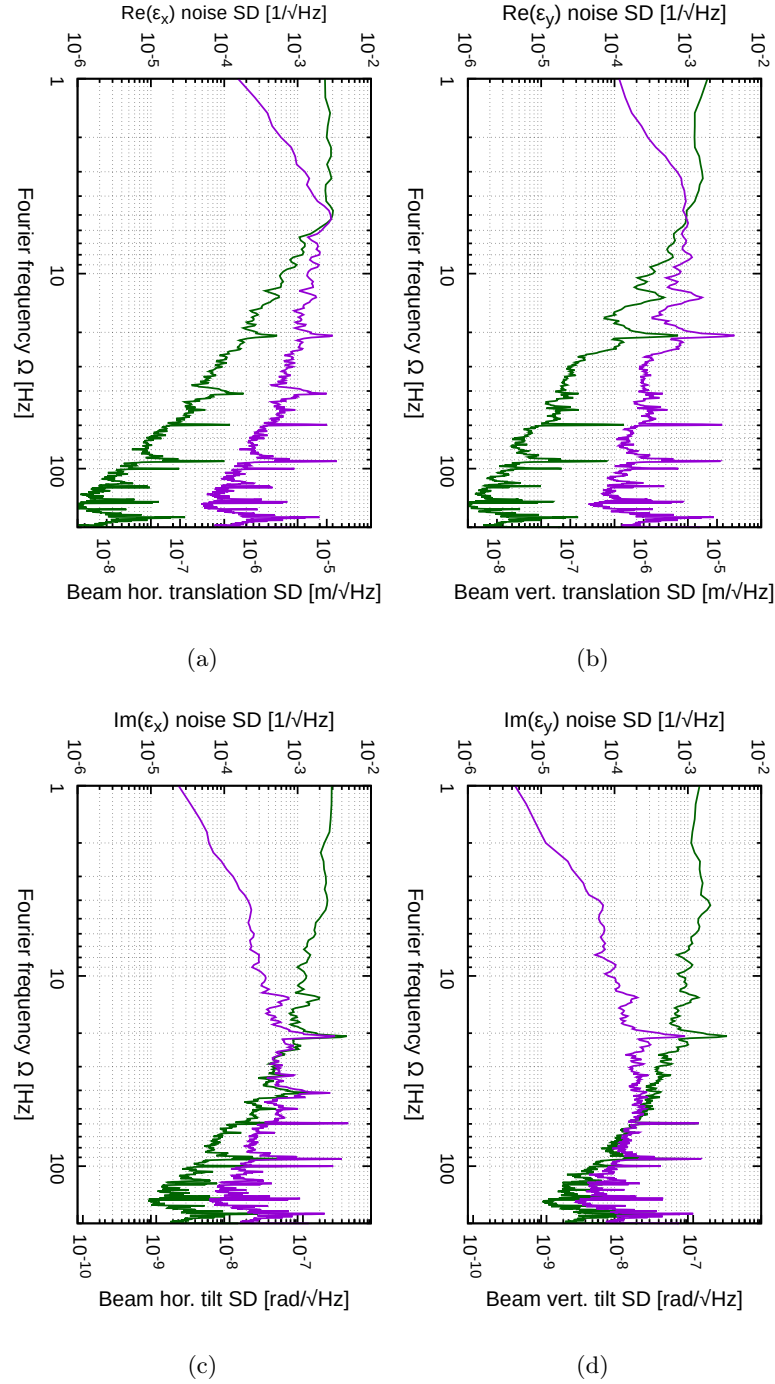
(a)

(b)

(c)

(d)

Figure 5.3: Noise spectral density of the horizontal and vertical ϵ parameter quadrature components over Fourier frequency for in-loop error-point noise (violet) and free-running noise projected from control signal (green) calculated from automatic alignment channels of the ALPS-II 20 m long cavity. The real quadrature of the horizontal (a) and vertical component (b) have been also calibrated as translation of the beam center, which is shown on the second axis of ordinates. The imaginary quadrature of the horizontal (c) and vertical component (d) have been calibrated as tilt angle around the cavity waist position, which is shown on the second axis of ordinates.

Bibliography

[1] S. A. Abel, M. D. Goodsell, J. Jaeckel, V. V. Khoze, and A. Ringwald. Kinetic mixing of the photon with hidden U(1)s in string phenomenology. *Journal of High Energy Physics*, 7:124, 2008.

[2] P. Arias, J. Jaeckel, J. Redondo, and A. Ringwald. Optimizing light-shining-through-a-wall experiments for axion and other weakly interacting slim particle searches. *Phys. Rev. D*, 82(11):115018, 2010.

[3] M. Betz. *The CERN Resonant WISP Search (CROWS)*. Dissertation, 2014.

[4] E. D. Black. An introduction to pound–drever–hall laser frequency stabilization. *American Journal of Physics*, 69(1):79–87, 2001.

[5] C. Bogan. *Stabilized High Power Lasers and Spatial Mode Conversion*. Dissertation, 2013.

[6] R. Bähre and others. Any light particle search II — Technical Design Report. *JINST*, 8:T09001, 2013.

[7] J. H. Christenson, J. W. Cronin, V. L. Fitch, and R. Turlay. Evidence for the 2π Decay of the K_2^0 Meson. *Phys. Rev. Lett.*, 13(4):138–140, 1964.

[8] R. J. Crewther, P. Di Vecchia, G. Veneziano, and E. Witten. Chiral Estimate of the Electric Dipole Moment of the Neutron in Quantum Chromodynamics. *Phys. Lett.*, B88:123, 1979. [Erratum: Phys. Lett.B91,487(1980)].

[9] T. Dafni, F. J. Iguaz, o. b. o. t. CAST, and IAXO collaborations. Axion helioscopes update: the status of CAST and IAXO. In *Proceedings of 3rd*

International Conference on Technology and Instrumentation in Particle Physics (TIPP 2014). Proceedings of Science, 2015.

[10] L. D. Duffy and K. van Bibber. Axions as dark matter particles. *New Journal of Physics*, 11(10):105008, 2009.

[11] K. Ehret et al. New ALPS results on hidden-sector lightweights. *Physics Letters B*, 689(4):149 – 155, 2010.

[12] First Sensor. First Sensor QP Data Sheet, 2011. url: `http://www.mouser.com/ds/2/313/QP5-6_TO_501040-586454.pdf`.

[13] Gonzalez-Cardel. Gaussian beam radius measurement with a knife-edge: A polynomial approximation to the inverse error function. *Appl. Opt.*, 52(16), 2013.

[14] O. W. Greenberg. CPT Violation Implies Violation of Lorentz Invariance. *Phys. Rev. Lett.*, 89(23):231602, 2002.

[15] H. Grote et al. The automatic alignment system of GEO 600. *Classical and Quantum Gravity*, 19(7):1849, 2002.

[16] G. Heinzel. *Advanced optical techniques for laser-interferometric gravitational-wave detectors*. Dissertation, 1999.

[17] G. Hernandez. *Fabry-Perot Interferometers*. Cambridge University Press, 1986.

[18] M. J. Herrero. The Standard Model. *ArXiv e-prints*, 1998. arXiv:hep-ph/9812242.

[19] P. W. Higgs. Broken Symmetries and the Masses of Gauge Bosons. *Phys. Rev. Lett.*, 13(16):508–509, 1964.

[20] R. Hodajerdi. *Production Cavity and Central Optics for a Light Shining through a Wall Experiment*. Dissertation, 2015.

[21] F. Hoogeveen and T. Ziegenhagen. Production and detection of light bosons using optical resonators. *Nuclear Physics B*, 358(1):3 – 26, 1991.

[22] D. Horns et al. Hardening of TeV gamma spectrum of active galactic nuclei in galaxy clusters by conversions of photons into axionlike particles. *Phys. Rev. D*, 86(7):075024, 2012.

[23] J. Isern. White dwarfs as physics laboratories: the case of axions. In K. Zioutas and M. Schumann, editors, *7th Patras Workshop on Axions, WIMPs and WISPs (PATRAS 2011)*, page 158, 2012.

[24] H. Kurashige. Highlight of Results from ATLAS at LHC. *Physics Procedia*, 80:14 – 18, 2015.

[25] P. Kwee. Charakterisierung von Lasersystemen für Gravitationswellendetektoren. Diploma thesis, 2005.

[26] G. Mueller, P. Sikivie, D. B. Tanner, and K. van Bibber. Detailed design of a resonantly enhanced axion-photon regeneration experiment. *Phys. Rev. D*, 80(7):072004, 2009.

[27] R. D. Peccei. QCD, strong CP and axions. *Journal of Korean Physical Society*, 29:S199–S208, 1996.

[28] R. D. Peccei and H. R. Quinn. Constraints imposed by CP conservation in the presence of pseudoparticles. *Phys. Rev. D*, 16(6):1791–1797, 1977.

[29] Planck Collaboration. Planck 2013 results. i. overview of products and scientific results. *Astronomy & Astrophysics*, 571:A1, 2014.

[30] J. H. Poeld. *Design, Implementation and Characterization of the Advanced LIGO 200 W Laser System*. Dissertation, 2014.

[31] G. G. Raffelt. Axions – motivation, limits and searches. *Journal of Physics A Mathematical General*, 40:6607–6620, 2007.

[32] A. Ringwald. Ultralight Particle Dark Matter. *ArXiv e-prints*, 2013. arXiv:1310.1256 [hep-ph].

[33] A. Ringwald. Axions and axion-like particles. *ArXiv e-prints*, 2014. arXiv:1407.0546 [hep-ph].

[34] A. Thuering and N. Lastzka. JamMt, 2011. Version 0.24, url: `http://www.sr.bham.ac.uk/dokuwiki/doku.php?id=geosim:jammt`.

[35] K. van Bibber and G. Carosi. First results from the Axion Dark Matter eXperiment (ADMX) upgrade. *Proceedings, 7th International Workshop on the Identification of Dark Matter (IDM 2008)*, IDM2008:068, 2008.

Lebenslauf

18.12.1981   geboren in Hannover

1988 - 1992   Besuch der Grundschule Mengendamm in Hannover

1992 - 1994   Besuch der Orientierungsstufe Edenstraße in Hannover

1994 - 2001   Besuch des Leibniz-Gymnasiums in Hannover
              Abschluss: Abitur

2002 - 2009   Studium der Physik an der Leibniz Universität Hannover
              Abschluss: Diplom

2011 - 2014   Stipendium der Max-Planck-Gesellschaft

2014 - 2016   wissenschaftlicher Mitarbeiter der Leibniz Universität Hannover
              am Institut für Gravitationsphysik

+++